An autocorrelation method for three-dimensional strain analysis

Christopher J. Thissen[*], Mark T. Brandon

Department of Geology and Geophysics, Yale University, New Haven, CT, USA

A B S T R A C T

We present a method of finite-strain estimation using the autocorrelation properties of deformed rock. Autocorrelation is the correlation of an image with itself as a function of an offset or lag. In two and three dimensions, the lag has both distance and direction. Many geologic materials are initially isotropic, which means that the autocorrelation function (ACF) will be initially isotropic as well. Deformation imposes an anisotropic distortion, which can be measured using the Ramsay and Fry strain methods for example, but can also be estimated from the ACF. X-ray tomography now provides a rapid way to measure the three-dimensional ACF of a geologic sample. Strain parameters are estimated by using a non-linear, best-fit method to minimize the anisotropy in the ACF. The ACF method works best for materials where the objects are internally uniform and contrast strongly with the matrix and other grains.

© 2015 Elsevier Ltd. All rights reserved.

"So fine was the morning except for a streak of wind here and there that the sea and sky looked all one fabric…" — Virginia Woolf, To the Lighthouse

1. Introduction

Geologists use the term fabric to refer to the spatial organization of features in a rock (e.g., Heilbronner and Barrett, 2013). Rocks will commonly contain primary fabrics, created at the time that the rock formed (e.g., bedding, cross-bedding, cumulate layering, etc.), and secondary fabrics, formed by metamorphism and deformation (e.g., metamorphic and melt segregation, foliation, lineation, crenulation, folds, boudins, shear bands, faults, etc.). The autocorrelation function (ACF) provides a generalized method for measuring the spatial dimensions and anisotropy of almost all rock fabrics (e.g., Panozzo Heilbronner, 1992; Heilbronner and Barrett, 2013).

Many methods of deformation analysis depend on statistical estimation of rock fabrics (e.g., Ramsay and Huber, 1983). In fact, if rocks lacked spatially organized fabrics, there would be no structure to analyze. The atmosphere on a sunny day is one example of a material that exhibits a lack of contrast. The atmosphere flows as a fluid, but on a clear day, it lacks any "memory" of its deformational history because the air lacks any visible internal structure. Similarly, a material where each point is independent of all other points, such as an image of white noise, also has no information about its deformational history (Fry, 1979). An atmosphere that contains both cloudy and clear air can preserve some information about its flow history. The reason is that the mixture of cloudy and clear air creates an internally correlated structure, in that particles within a cloud are likely to be found near other cloud particles, and clear air particles are likely to be found near other clear air particles. The ACF provides a generalized method to quantify both the magnitude and orientation of this correlation.

Our objective here is to relate ACF measurements to strain. Thus, it is important to note that the ACF method, like many strain methods, requires well-understood features that are statistically isotropic in the initial state and respond passively to deformation. As with many strain methods, the success of the measurements depends on finding samples that are consistent with these requirements.

Panozzo Heilbronner (1992) was first to propose using the ACF for measuring finite strain. The approach has become more appealing given the availability of X-ray tomography (e.g., Fusseis et al., 2014), which directly images the three-dimensional fabric of a rock. Note that we use the term "image" in a generic sense to mean any two-dimensional (2D) or three-dimensional (3D) field. In X-ray tomography, the features in the rock are represented by the spatial variation in X-ray attenuation. A 3D attenuation field provides an ideal image for estimating autocorrelation in rock samples.

For granular materials, deformation creates a directional

---

* Corresponding author. Department of Geology and Geophysics, Yale University, PO Box 208109, New Haven, CT 06520, USA.

    E-mail address: christopher.thissen@yale.edu (C.J. Thissen).

variation in grain diameter. The ACF reveals this fabric as a directional variation in the ACF length scale. In the simplest case, the axial ratio of the contours of the ACF equals the axial ratios of the grains (Lado and Torquato, 1990; Torquato and Lado, 1991; Panozzo Heilbronner, 1992). Panozzo Heilbronner (1992) estimated finite strain by measuring the ellipticity of contours of the ACF. Others have considered how the ACF varies spatially throughout the sample and also as a function of lag (Heilbronner, 2010; Svitelman and Dinariev, 2013).

We build on this previous work in three ways. First, we introduce a generalized best-fit method for estimating the anisotropy of the ACF determined from a 2D or 3D image. Second, we develop a method for estimating the uncertainties associated with the estimated parameters. Third, we consider both theoretical and practical aspects for implementing this method to measure strain. Our analysis of the ACF depends, in part, on the type of data analyzed, and so we begin with an overview of X-ray tomography.

2. X-ray tomography

X-ray tomography provides a 3D image of the X-ray attenuation structure of an object at a micron scale (Maire and Withers, 2014). The time required to image a sample is beam-line dependent, but ranges from several hours to 10 min or faster (Rivers et al., 1999). X-ray tomography requires limited sample preparation (e.g., Lindquist and Venkatarangan, 2000; Fusseis et al., 2014). It is non-destructive, which is ideal for rare or valuable samples (e.g., Rivers et al., 1999; Ketcham and Carlson, 2001; Ebel and Rivers, 2007), and for samples where other complementary analyses are needed (e.g., figure 1 in Hu et al., 2014). The following papers provide an introduction to the method: Denison et al. (1997); Denison and Carlson (1997); Ketcham and Carlson (2001); Sutton et al. (2002); Carlson (2006); Jerram and Higgins (2007); Baker et al. (2012); Cnudde and Boon (2013); Fusseis et al. (2014); Maire and Withers (2014). Sample preparation, experimental design, choosing an appropriate photon source, and image reconstruction are reviewed by Reeder and Lanzirotti (2006) and Fusseis et al. (2014).

X-ray attenuation is a scalar field variable, meaning it is a single quantity that varies spatially throughout the sample volume. A tomographic image, or tomogram, is represented by discrete attenuation estimates at nodes within a 3D grid. Each node lies at the center of a volume element called a voxel, which is the 3D equivalent of a pixel (Carlson, 2006). The attenuation coefficient reported in each voxel is the average attenuation within the voxel (Hubbell and Seltzer, 2004; Gualda et al., 2010).

X-ray attenuation varies throughout a heterogeneous sample. The example shown in Fig. 1 is a $1392 \times 1392 \times 1$ voxel slice from the $1392 \times 1392 \times 1040$ voxel grid that spans a full sample volume. Attenuation is represented by a grayscale intensity ($1-256$), with white (256) representing the largest attenuation. Note that the region surrounding the sample is black because air has minimal attenuation.

The attenuation coefficient, μ, is defined by

$$\mu = -\frac{1}{I}\frac{dI}{ds} \tag{1}$$

where s is the path length of the X-ray beam, and I is the X-ray intensity (Hubbell and Seltzer, 2004). X-ray tomography is able to easily resolve features with attenuation coefficients that differ by more than a factor of two (Ebel and Rivers, 2007; Gualda et al., 2010). The coefficient μ scales linearly with density and as a power law with atomic number (e.g., Denison et al., 1997). Several calculators are available for estimating μ (Hubbell and Seltzer,
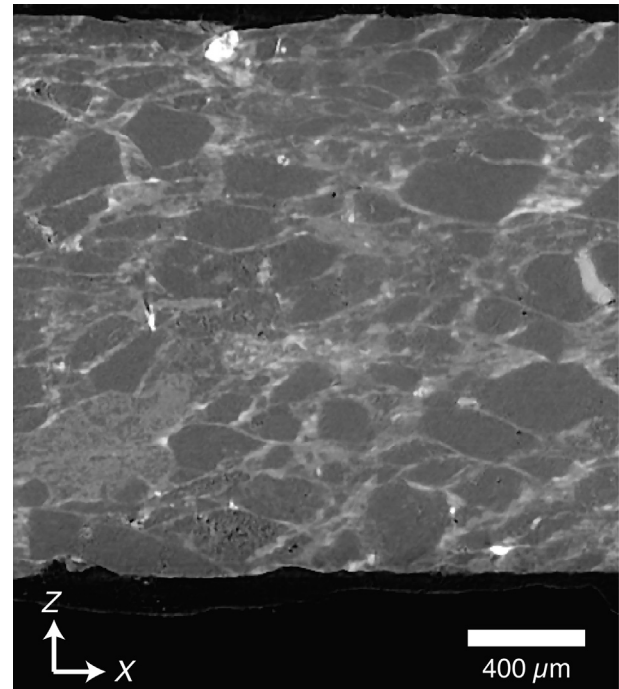

Fig. 1. X-ray tomography image of an $X–Z$ section through a sandstone deformed by pressure solution (sample 92810-3 from the Olympic subduction complex in NW Washington State). A deformation fabric is indicated by detrital grains (dark gray), which are separated by anastomosing cleavage surfaces (long, thin light-gray features, approximately parallel to the X direction) and by directed overgrowths (thicker light-gray features, oriented in the X direction). The cleavages have accommodated shortening in the Z direction, and the overgrowths, extension in the X direction.

2004; Chantler et al., 2005; Berger et al., 2010; MuCalc spreadsheet: http://www.ctlab.geo.utexas.edu/software/index.php). Combining X-ray attenuation with other kinds of data can further improve image resolution (Huddlestone-Holmes and Ketcham, 2005; Boone et al., 2011). X-ray tomography requires that the total attenuation through the sample is no more than 80% (Gualda et al., 2010), so suitable rock samples are commonly on the order of centimeters in size. A contrast in attenuation coefficients, rather
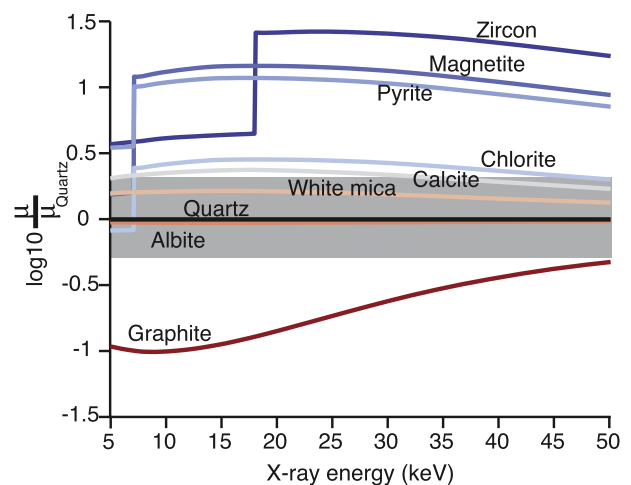

Fig. 2. X-ray attenuation coefficients for various geologic materials (Chantler et al., 2005), as normalized by the coefficient for quartz. The gray regions show a factor of two range for an attenuation coefficient relative to that for quartz. Minerals that lie outside that range are easily resolved relative to quartz in an X-ray tomogram.

than the absolute value, is important for successfully imaging fabrics using X-ray tomography. For example, most minerals have a strong contrast with quartz except for feldspar (Fig. 2). The X-ray beam energy can be adjusted to improve the contrast for some minerals. The large jumps in the attenuation value are absorption edges, and correspond to the ejection of electrons from specific electron shells (Gualda et al., 2010).

Many software programs have been developed to analyze 3D tomography data for geologic materials: Quant3D (Ryan and Ketcham, 2002; Ketcham and Ryan, 2004), Blob3D (Ketcham, 2005a; 2005b), Ctsta (Liu et al., 2009), WinDICOM (O'Connor et al., 2009), Morpho+ (Brabant et al., 2011), Pore3D (Brun et al., 2010), PhaseQuant (Elangovan et al., 2012), YaDiv (Friese et al., 2013). Fusseis et al. (2014) reviews these programs in more detail. In particular, Ketcham (2005a; 2005b) provides a way to isolate the shape of segmented phases and analyze them for strain estimates. Some authors have highlighted difficulties in estimating parameters using segmentation methods (e.g., Iaasonov et al., 2009; Baveye et al., 2010; Iassonov and Tuller, 2010; Andrä et al., 2013). Our method avoids these problems by using a statistical description of the entire sample, independent of actual grain boundaries.

3. The autocorrelation function

To provide a more intuitive understanding of the ACF, we begin by considering a few qualitative examples. Fig. 3a shows an average of yearbook photos for high-school women in the 1967 class in Fort Worth, Texas (Salavon, 1998). The individuals are unrecognizable, but the average shows a clear structure that is immediately identifiable as a generic portrait. The average also shows hints about the dress and hairstyle typical for 1967.

Similarly, Fig. 3b shows an average of 200 tomogram slices, or approximately 392 μm, for the sandstone sample in Fig. 1. If the image volume had no correlated structures (e.g., no grains or foliation), then each pixel in the image would be independent of all the other pixels, and the average image in Fig. 3b would be a statistically uniform shade of gray. However, the image shows areas with distinct pixel intensities, which indicate spatial correlations over the 200 slices.

Considering autocorrelation more formally, the ACF is represented by the notation $\rho(\mathbf{r})$, where the lag vector $\mathbf{r}$ indicates the offset between the image and its copy, and the autocorrelation statistic ρ is a measure of the overall similarity of the images in this offset relationship. ρ is limited to the range -1 to $+1$. A value of $+1$ means that the image and its offset copy match exactly, at a pixel or voxel level (i.e. perfect correlation). A value of 0 means that the image and its offset copy have no statistical similarity. A value of -1 means that the image and its offset copy are complete opposites (i.e., perfect anticorrelation). The ACFs for most real images usually range from 0 to $+1$.

Several simple examples illustrate basic features of the ACF (Fig. 4). The examples are composed of two phases, which appear as black circles surrounded by a white background. It is helpful to envision the autocorrelation at a specific lag as the overlapping area of the black circles in two identical, offset sheets (Panozzo Heilbronner, 1992). However, when the ACF is calculated, the image is rescaled so that the mean and standard deviation of the intensity values are zero and one, respectively. Thus, the ACF makes no distinction between the phases. Visually, we might consider the white phases to be the background or the matrix in Fig. 4, but the ACF is only sensitive to the contrast between the phases and the relative abundance of the phases.

The first example (Fig. 4a) has a single circle, which can be viewed as a "dilute phase", in that the black circle occupies a very small area in the total aggregate. This example is analogous to sparse amygdules or phenocrysts in a volcanic rock. The ACF for this example ("Single Circle" in Fig. 4d) starts with $\rho = 1$ at $r = 0$ and decreases to zero at $r = 2R$ where R is the radius of the circle. The reason is that the black phase is dilute enough that the only correlation is "self-correlation", where objects still overlap with their offset copies.

The second example (Fig. 4b) has a square lattice of periodically repeating circles, arranged with a uniform distance $4R$ between the centers of each circle in the horizontal and vertical directions. The
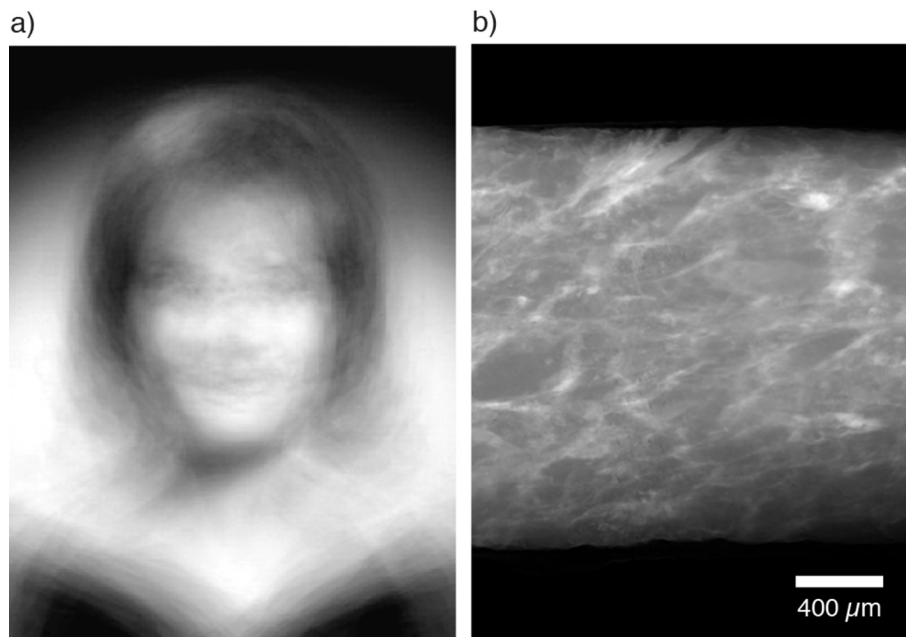

a)   b)

Fig. 3. Correlated structure as illustrated using averaging. (a) An average of yearbook pictures for women in the 1967 graduation class at Fort Worth High School (Salavon, 1998). (b) An average of 200 X–Z sections from an X-ray tomogram of deformed sandstone, representing an out-of-plane thickness of 392 μm (sample 92810-3 from the Olympic subduction complex).
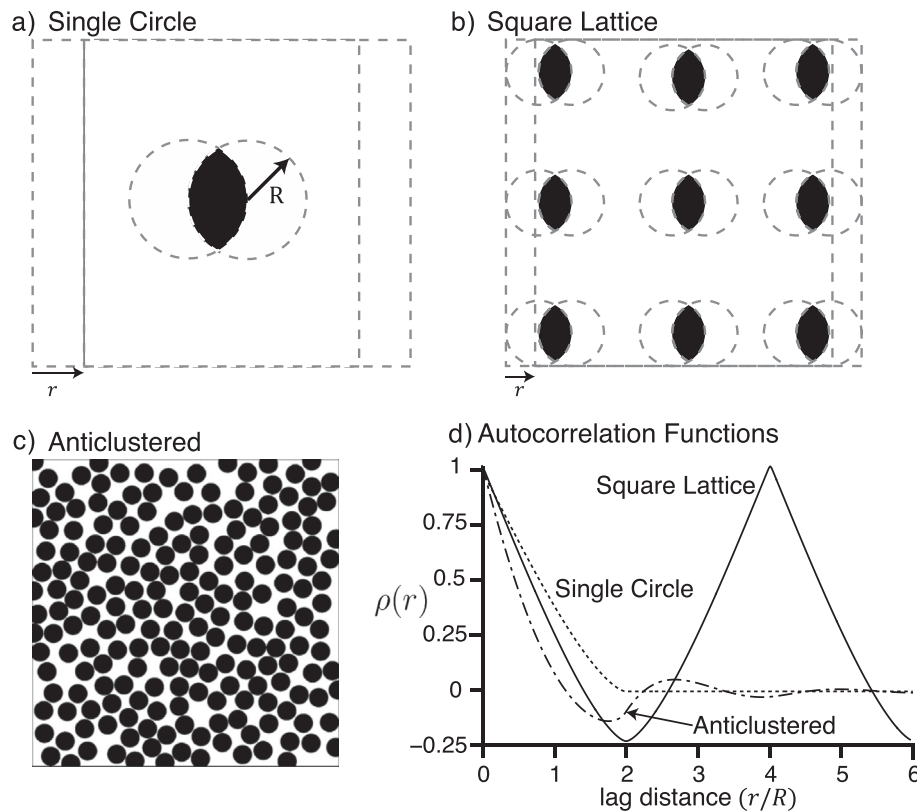
Fig. 4. The autocorrelation function for three examples: (a) a single circle, (b) a square lattice of circles, and (c) an anticlustered distribution of circles. (d) The autocorrelation function $\rho(r)$ for these examples is related to the change in the overlapping area of the circles, which is set to 1 when the lag $r = 0$, and decreases as the lag increases to R, the radius of the circles.

ACF for this example is shown only for the image horizontal direction ("Square Lattice" in Fig. 4d). This example has two important differences from the "Singe Circle" example. First, the circles in this example compose a much greater fraction of the image. As a result, the black circles and white background have opposite signs in the rescaled image, and have negative autocorrelation values where the circles and matrix overlap. This anticorrelation is expressed by the shorter decay lengthscale of the "Square Lattice" ACF compared to the "Single Circle" ACF, and by the negative autocorrelation values near $r = 2R$ and $r = 6R$.

Second, the "Square Lattice" ACF also has additional maxima at $r = 4nR$, where $n = 1, 2, \ldots \infty$ (Fig. 4d shows the first of these maxima at $r = 4R$). These maxima correspond to "neighbor-correlation" caused by overlap between neighboring circles (c.f., blocking-function, Torquato, 2002). For this example, the self-correlation and neighbor-correlation parts of the ACF are well separated because the lattice spacing, $4R$, is much larger than the diameter, $2R$, of the circles.

The third example (Fig. 4c) has an irregular set of anticlustered circles, which are meant to represent grains in a rock. Natural grains have an irregular (i.e., non-periodic) arrangement and are anticlustered, meaning they do not physically overlap. In addition, the shapes and placement of the objects are statistically isotropic, meaning that there is no significant dependence on direction. Thus, the ACF ("Anticlustered" in Fig. 4d) is solely dependent on the offset distance, $r = |\mathbf{r}|$.

The ACF for this example shows a shorter decay lengthscale at short lags ($r < R$) when compared to the previous examples. As before, this results from anticorrelation between the black circles and white background. This example also shows a decaying periodic pattern at long lags ($r > R$). The ACF is similar to that for the

Square-Lattice example, except for the fact that the self-correlation and neighbor-correlation parts of the ACF now overlap. This overlapping is expected in natural geologic materials, where the spacing between grain centers is similar to the diameter of the grains.

The anticlustered condition creates a decaying periodicity in the ACF, with a wavelength proportional to the diameter of the circles. In statistical mechanics, this problem is commonly treated using the pair-correlation function (Debye et al., 1957; Torquato and Stell, 1982, 1983, 1985). The pair-correlation function gives the probability of finding a particle center at a lag r from a reference particle center. The density of points in a Fry diagram (Fry, 1979) is proportional to the probability provided by the pair-correlation function. Note that the peak at $r/R = 2.5$ in the "Anticlustered" curve in Fig. 4d corresponds to the high-density girdle in the nearest-neighbor distribution of a Fry plot (Fry, 1979; Panozzo Heilbronner, 1992). Torquato (2002) has a detailed review of this topic.

In the Introduction, we mentioned that there are cases where a material might lack a spatially organized fabric. The next two examples highlight end-member cases. The examples are so simple that illustrations are not needed. The first is a material with only one phase. The image would have a uniform intensity, so ρ would be everywhere 1, regardless of the lag. This example is analogous to a monomineralic rock. Of course, a monomineralic rock might be composed of grains with different crystal orientations, as determined, for example, by electron backscatter diffraction. For this case, the "phases" could be defined on the basis of orientation, and a standard ACF analysis would then be possible. The second example is a two-phase material, where one phase is distributed randomly as infinitesimal grains. In practical terms, infinitesimal would mean a grain that is near the size an individual pixel or voxel.

For this example, $\rho = 1$ at $r = 0$, but drops to $\rho = 0$ for $r > 0$.

We now consider the effects of deformation on autocorrelation. The ACF contains information about both particle shapes and neighbor distances, and the focus here is to distinguish between the deformation of particles, as measured by Ramsay's (1967) R_f/ϕ method, and the deformation of nearest-neighbor distances, as measured by the Fry (1979) method.

For the first example (Fig. 5a–b), consider a 2D aggregate composed of regularly spaced black ellipses with the short axis R_Y equal to half the length of the long axis R_X. The spacing is isotropic, meaning that the distances between ellipse centers are the same in both the horizontal and vertical directions. The influence of anisotropy on the ACF is indicated by different decay length scales: ρ reaches zero at lag $r/R_Y = 2$ for the Y direction, and at $r/R_Y = 4$ for the X direction. The ratio of these two decay length scales is equal to the axial ratio of the ellipses. We use the term "Ramsay effect" to describe this anisotropy of ρ associated with self-correlation of particle shapes. The ACFs for the X and Y directions show a second maxima at the same lag, $r/R_Y = 8$, which means that the neighbor correlation is isotropic. The Fry method would show zero strain for this case.

Now consider the second anisotropic example (Fig. 5c–d), where circles with radius R are arranged on an anisotropic grid, such that the object centers are spaced $6R$ apart in the X direction, and $4R$ in the Y direction. The ACF is isotropic for self-correlation. In other words, the length scale for initial decay of ρ is the same, regardless of orientation. Ramsay's R_f/ϕ method would find zero strain for this example. Note, however, that ρ increases back to one at $r/R = 6$ in the X direction and $r/R = 4$ in the Y direction. In other words, ρ is isotropic for self-correlation but anisotropic for neighbor-correlation. Thus, we use the term "Fry effect" to describe the anisotropy of ρ due to the distribution of neighboring grains.

The last set of examples (Fig. 6) are based on a 2D aggregate made up of three phases, rendered in black, gray, and white, and assigned image intensities of 10, 1, and 0, respectively. The objective is to show how the ACF is affected when more than two phases are present. The first example (Fig. 6a–b) has large black elliptical grains with vertical long axes, and small gray elliptical grains with horizontal long axes. The full 2D ACF is shown as contours of ρ as a function of the x and y components of the lag vector. All of the ρ contours have the same elliptical shape as the black grains. The reason is that black grains are large in size and have a large contrast with the other intensities, so the ACF is strongly weighted towards the grain shapes for this phase.

The second example (Fig. 6c–d) shows what happens when the gray and black phases are exchanged. The black elliptical grains are now small, but they still have a strong contrast relative to the other two phases. The 2D ACF shows that, at short lags, the ρ contours have an elliptical shape similar to that for the black grains. As the lag distance increases, the ρ contours transition to an elliptical shape similar to that of the large gray grains. The gray grains are larger in this example, which compensates for its low contrast relative to the white phase, but only at long lengthscales.

This example highlights a subtle feature of autocorrelation for images with a range of grayscale intensities. The ACF is more heavily weighted towards features that have a strong contrast relative to the rest of the image. As a result, image processing methods can be used to weight the ACF towards specific features of
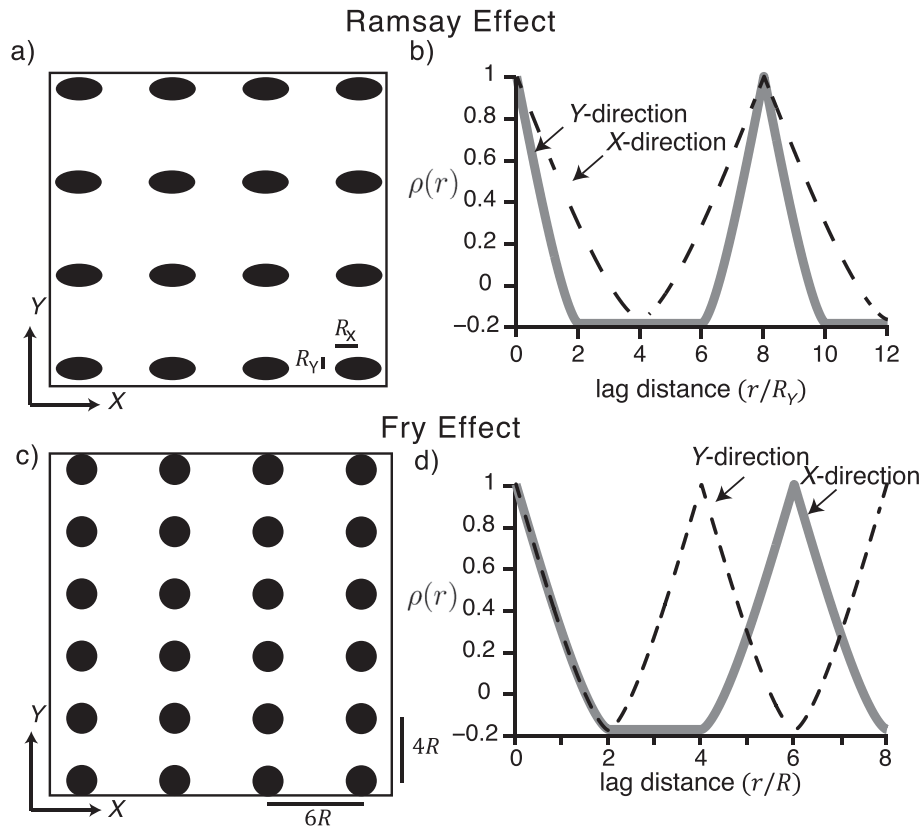

Fig. 5. The Ramsay and Fry effects in the ACF. (a, b) At short lags, where $r/R < 1$, the ACF represents the correlation of features with themselves, and thus the ACF is sensitive to the anisotropy of features. The anisotropy in this range is similar to that measured by the Ramsay method, which is focused on the distortion of features. (c, d) At long lags, where $r/R > 1$, the ACF is sensitive to the anisotropic distribution of features with respect to each other. This anisotropy is similar to that measured by the Fry method, which focuses on the distribution of nearest neighbors.
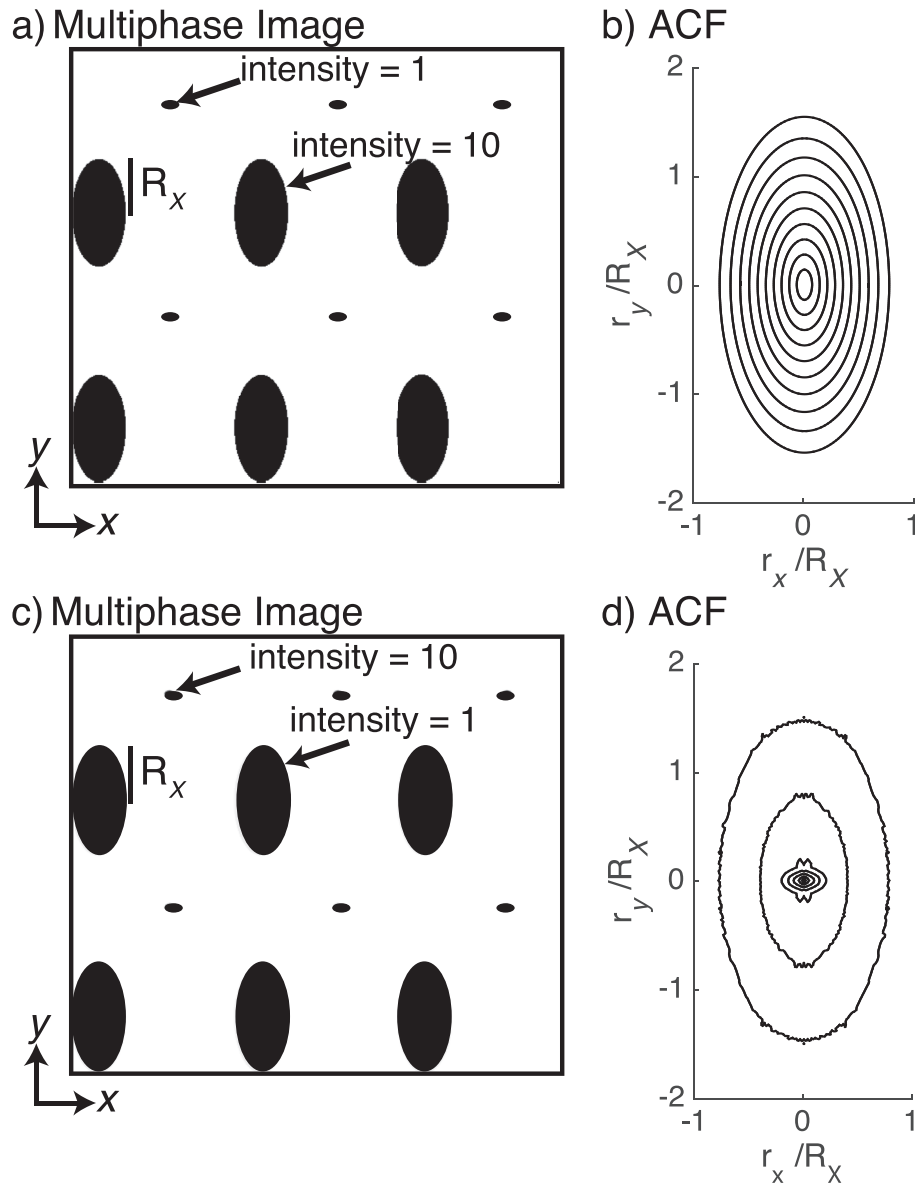
a) Multiphase Image

b) ACF

c) Multiphase Image

d) ACF

Fig. 6. Two examples showing how the ACF is affected by the contrast in intensity between phases. The ACFs for these examples are shown as contours of ρ in terms of x and y components of the lag vector and a contour interval of 0.1. (a) For the first example, the gray ellipses are small and have little contrast with the surrounding white phase, so (b) the ACF contours everywhere mimic the anisotropy of the larger black ellipses. (c) For the second example, the black ellipses are small, but have high contrast with respect to the other two phases. (d) As a result, the ACF contours have the same elliptical shape as the black phase at short lags ($r/R_X \sim 0.1$), but take on the elliptical shape of the gray phase at long lags ($r/R_X > \sim 0.3$).

the fabric. Useful methods potentially include gamma correction or image segmentation (e.g. Heilbronner and Barrett, 2013). Remember, however, that the image is standardized before calculating the ACF. As a result, the ACF is unaffected by linear rescaling of the image intensities (Panozzo Heilbronner, 1992).

4. Estimating grain size in the ACF

Grain size is a significant parameter in its own right, but it is especially important for distinguishing between self-correlation and neighbor-correlation. There are several ways to estimate the average grain radius. To guide this discussion, we generated a 3D aggregate composed of non-overlapping, close-packed, identical black spheres set in a white matrix (Fig. 7a). (The numerical method is described in Section 7.1.) The circles vary in size, but this result is

simply due to sectioning through the 3D spheres, which otherwise have a uniform radius $R = 1$. The ACF for the full 3D volume as a function of radial lag exhibits both self-correlation and neighbor-correlation (Fig. 7b). The spheres in this example compose 54% of the volume.

Debye and Bueche (1949) proposed an exponential model for the ACF as determined from X-ray scattering of atomic-scale vacancies

$$\rho(r) = \exp(-r/R_C) \tag{2}$$

where R_C is the characteristic lag for the decay of ρ with increasing r. Maätzler (2002) showed that the characteristic lag R_C of the ACF for an aggregate of identical overlapping spheres is equal to the radius of the spheres. Debye et al. (1957) estimated R_C using the derivative of the ACF at $r = 0$. For (2), this estimate is $R_C \approx -(\mathrm{d}\rho(r = 0)/\mathrm{d}r)^{-1}$.
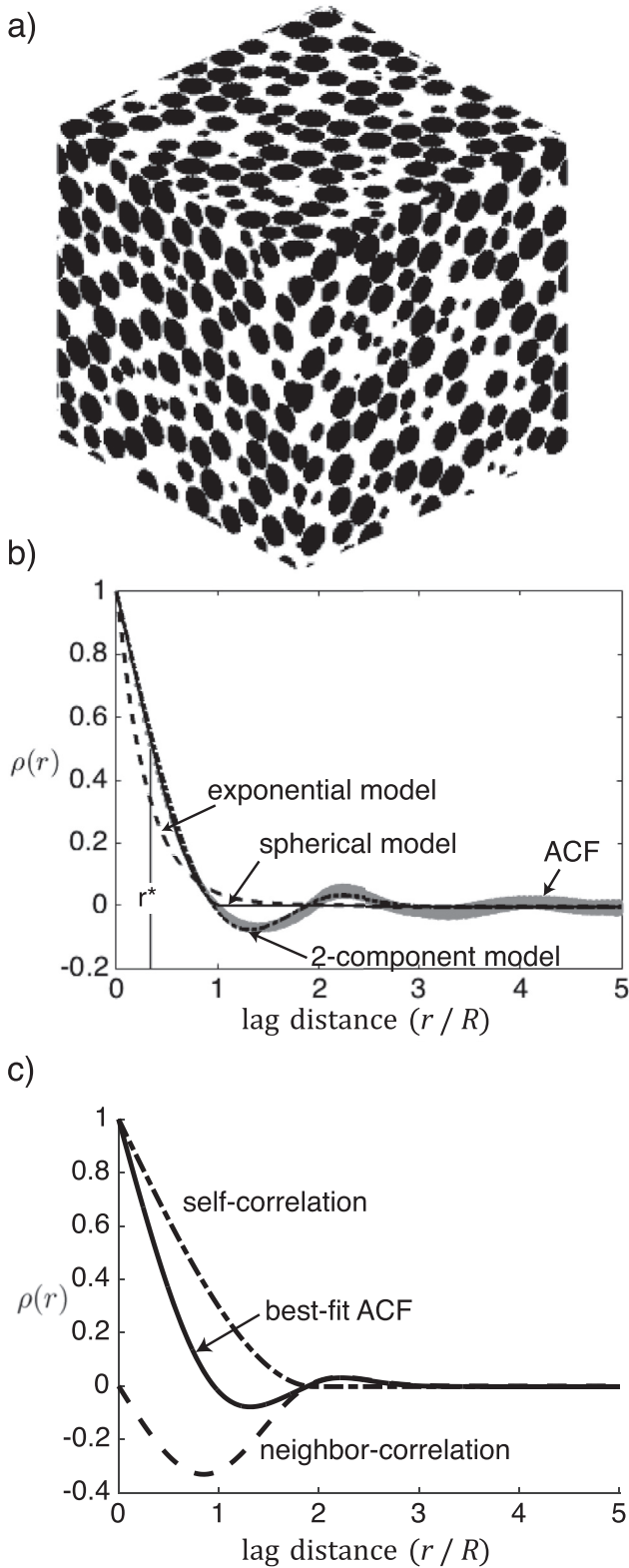
a)

b)

c)

Fig. 7. Comparison of ACF model functions. (a) A 3D synthetic aggregate composed of non-overlapping identical spheres. (b) The ACF for the synthetic aggregate (gray line) and best-fit solutions using the exponential model (dash line), the spherical model (solid line), and the 2-component model (dash-dot line). The "half-height" lag is shown by r^*. (c) The best-fit 2-component model (solid line) and the self-correlation (dash-dot line) and neighbor-correlation (dash line) components for that fit.

An alternative is to estimate the parameters in (2) using a least-squares fit to the ACF (Maätzler, 2002). Neither approach is satisfactory. The derivative method emphasizes only a small fraction of the ACF, and the least-squares approach has problems separating self-correlation from neighbor-correlation. This point is illustrated in Fig. 7b, which shows the poor fit of the exponential model to the ACF of the simulated aggregate. The best-fit estimate $R_C = 0.31$ is much smaller than the expected value, $R = 1$.

A different approach approximates the grain size by using a characteristic point in the short-lag part of the ACF (Panozzo Heilbronner, 1992; Buscombe et al., 2010). The convention is to use the "half-height lag", r^*, which is the lag where ρ first drops to 0.5. Panozzo Heilbronner (1992) estimated that the average grain radius is given by $\overline{R} \approx 1.5r^*$. Based on extensive calibration between the ACF and measurements for images of unconsolidated sediments, Buscombe et al. (2010) recommended that $\overline{R} \approx \pi r^*$.

Another approach to estimating grain size is the spherical model, which refers to the idealized ACF for self-correlation of a single sphere (p. 79 in Torquato, 2002)

$$\rho(r) = (r \leq 2R)\left(1 - \frac{3}{4}\frac{r}{R} + \frac{1}{16}\left(\frac{r}{R}\right)^3\right) \tag{3}$$

Note that the logical expression $(r \leq 2R)$ equals 1 if true and 0 if false. Substitution of $\rho(r^*) = 0.5$ into (3) gives

$$\overline{R} = 1.44r^* \tag{4}$$

which is nearly identical to the estimate of Panozzo Heilbronner (1992).

In our experience, all of these approximations work poorly for dense aggregates. As an example, the simulated aggregate has $r^* = 0.35$. Thus, the approximations above predict average grain radii of 0.50, 0.53, and 1.10. These approximations are crude, in part because they do not account for neighbor-correlation. The method suggested by Buscombe et al. (2010) gives the closest approximation to the true value of one. This is probably because our grain-supported aggregate is similar to the unconsolidated sediments on which the recommendation is based. Buscombe et al.'s method will diverge from the true radius for materials that cannot be approximated as unconsolidated sediments.

To overcome these issues, we propose a generalized two-component model for the isotropic ACF

$$\rho(r) = (r \leq 2R_S)\left(1 - \frac{3}{4}\frac{r}{R_S} + \frac{1}{16}\left(\frac{r}{R_S}\right)^3\right)$$
$$+ f_N \exp\left(-\left(\frac{r}{R_N}\right)^\beta\right)\sin\left(\frac{\pi r}{R_N}\right) \tag{5}$$

where the self-correlation component of the ACF is represented by (3) and the neighbor-correlation component, by a sinusoid with a decaying amplitude (modified from equation (7) in Cule and Torquato, 1999). This model has four unknown parameters: R_s, f_N, R_N and β. R_S represents the length scale for self-correlation, and thus is representative of the average grain radius. f_N defines the amplitude of the neighbor component. Note that f_N can be negative for multi-phase aggregates, given that neighboring phases are likely to have different intensity values. The neighbor component has two parts. The decay of the neighbor-correlation with r is represented by a stretched exponential function, where R_N defines the decay length scale and the power β defines the amount of stretching of the exponential function. We have found that β values other than one are needed to ensure a good fit to an isotropic ACF. The periodicity for the neighbor-correlation is represented by the

sin function, which has a wavelength of $2R_N$. Torquato (2002, Chapter 5) discussed a variety of analytical solution for ACFs for simple aggregates. Equation (5) does include the spherical model for self-correlation, but it is otherwise empirical in its derivation. The advantage is that the two-component model is relatively simple and thus much easier to use for estimation.

The unknown parameters for (5) can be estimated using a nonlinear least-squares routine, such as the one discussed below for strain estimation. We have found that the analysis works best by using the Fisher transform to convert ρ to ζ, which has more uniform variance with r (see below for details). The starting estimates for R_S and R_N are set to be about five times larger than $\bar{R}$, as determined from (4). This strategy is important for avoiding local minima for the best-fit solution. Starting estimates for β and f_N are set to 1 and 0, respectively. R_S and R_N are constrained to be positive.

The two-component model gives a best-fit solution for the synthetic example of $R_S = 0.97$, which compares well with the true value of 1. The estimates for the other parameters are $f_N = -0.36$, $R_N = 1.89$, and $\beta = 3.41$. The fit has an $R^2 = 0.82$. We use the F ratio test of Bevington and Robinson (2003, p. 207) to compare the fit provided by the two-component model and the spherical model. In all cases, the two-component model provides a significantly better fit.

Fig. 7c shows the best-fit ACF, along with the predicted components for self-correlation and neighbor-correlation. The ACF is dominated by the self-correlation component, but both components are significant at short lags, $0 < r/R < 2$. The neighbor-correlation component commonly decays to zero by $r/R = 5$. Thus there is little need to analyze the ACF beyond that point.

5. Estimating the autocorrelation function

Consider the general case for an image, where $U(x, y, z)$ are continuously varying scalar values within a 3D domain spanned by x, y, and z. We focus here on X-ray attenuation, but the scalar field can be anything that characterizes the material in that domain. Our objective is to estimate the autocorrelation for this field variable as a function of the components of the lag vector, r_x, r_y, and r_z. We introduce a standardized variable U_S defined by

$$U_S = \frac{U - c}{\sigma(U - c)} \qquad (6)$$

where c is the mean value for U and $\sigma(U-c)$ is the standard deviation of U around the mean. The standardization in (6) ensures that ρ remains within the limits of ± 1. The ACF is defined using U_S (Priestley, 1981),

$$\rho(r_x, r_y, r_z) = \int_V U_S(x, y, z) U_S(x - r_x, y - r_y, z - r_z) \mathrm{d}x\, \mathrm{d}y\, \mathrm{d}z. \qquad (7)$$

and the integral is over the volume V.

The ACF is simply a cross-correlation of the field variable with a copy that is offset by r_x, r_y, and r_z. Equation (7) provides a formal definition, but it is too cumbersome to serve as a method of calculation.

The Fourier transform provides a faster way to calculate the ACF. We start with a discrete uniform grid of standardized attenuation values, $U_S(j_x, j_y, j_z)$, where Δ is the grid spacing, and $j_x = 0$ to $N_x - 1$, $j_y = 0$ to $N_y - 1$, and $j_z = 0$ to $N_z - 1$ are space-domain indices in the x, y, and z directions. The Fourier transform is used to convert the grid into the wave domain. The Fourier coefficients are given by

$$\mathscr{U}_S(k_x, k_y, k_z) = \mathscr{F}\left(U_S\left(j_x, j_y, j_z\right)\right) \qquad (8)$$

where $\mathscr{F}$ and $\mathscr{F}^{-1}$ are operators that indicate the Fourier transform and its inverse, and $k_x = 0$ to $N_x - 1$, $k_y = 0$ to $N_y - 1$, and $k_z = 0$ to $N_z - 1$ are wave-domain indices in the x, y, and z directions. Keep in mind that the Fourier coefficients $\mathscr{U}(k_x, k_y, k_z)$ are, in general, complex valued.

The Fourier coefficients of the ACF are determined by the products

$$\mathscr{R}(k_x, k_y, k_z) = \mathscr{U}_S(k_x, k_y, k_z)\, \mathscr{U}_S^*(k_x, k_y, k_z) \qquad (9)$$

where $*$ indicates the complex conjugate. The inverse Fourier transform is used to return the ACF to the space domain,

$$\rho\left(j_x, j_y, j_z\right) = \mathscr{F}^{-1}\left(R(k_x, k_y, k_z)\right) \qquad (10)$$

Consider the following MATLAB example, where imageFile.tif is 2D grayscale image file accessible in the current directory. The image should have an odd number of pixels in each dimension.

```
1. U = double(imread('imageFile.tif'));
2. c = mean(U(:));
3. Us = (U-c)/sqrt(mean((U(:)-c).^2));
4. N = numel(U);
5. Uscript = fftn(Us)/N;
6. Rscript = Uscript.*conj(Uscript);
7. Rho = fftshift(ifftn(Rscript)*N);
8. [nx,ny] = size(U);
9. rx = linspace(-(nx-1)/2,(nx-1)/2,nx);
10. ry = linspace(-(ny-1)/2,(ny-1)/2,ny);
11. [Ry,Rx] = ndgrid(rx,ry);
12. r = sqrt(Rx.^2 + Ry.^2);
13. figure; plot(r(:), Rho(:), '.');
14. figure; pcolor(Rx, Ry, Rho); shading interp; axis equal;
```

Line 1 loads the image into the matrix U and converts the values to double precision. Lines 2 and 3 standardize the matrix. Lines 4–7 calculate the ACF, and lines 8–12 calculate the x and y lag components in units of pixels. Line 13 plots the ACF as a function of lag distance. Line 14 plots the ACF as a 2D color map. Note that the "fftshift" command in line 7 organizes the matrix Rho so that the zero lag, $r = 0$, is located at the central pixel.

There has been a lot of discussion about how to reduce bias and increase precision when estimating the ACF (e.g., Priestley, 1981; Broersen, 2006). For our study of fabrics, we are not as interested in the true values of the autocorrelation, but rather the anisotropy of the autocorrelation. As such, we have found that the Fourier method, which has been criticized as less than optimal for estimating the true values of the ACF (Broersen, 2006), does the best job preserving sample anisotropy. Windowing functions are commonly used in conjunction with the finite Fourier transform to reduce edge effects and enhance spectral resolution (e.g., Press et al., 2007, p. 656–660). Our tests using various windowing filters have found that typical windowing functions, such as the Hann filter, generate artificial anisotropy in the sample, which causes biases in the estimated deformation parameters. Sample anisotropy is best preserved by calculating the ACF from the untreated standardized image. (Of course, the image has already been delimited (i.e., windowed) to finite dimensions.) The edges of the image do generate some ringing (i.e., the Gibbs effect), but this ringing appears to contribute relatively little to the ACF (also see Panozzo Heilbronner, 1992).

6. Estimating deformation parameters

To estimate the deformation parameters from a sample ACF, we

search for a stretch tensor that reduces the ACF to an isotropic form. The assumption, one that is used in almost all strain methods, is that the fabric of the material was isotropic before deformation.

The deformation of a material line is defined by

$$\mathbf{r} = \mathbf{VRr}_0, \tag{11}$$

where $\mathbf{V}$ is the left-stretch tensor, $\mathbf{R}$ is a rotation tensor, and $\mathbf{r}_0$ and $\mathbf{r}$ are vectors representing the material line before and after the deformation. For geologic studies, there is generally little information about $\mathbf{R}$. Thus, the estimation is focused solely on the stretch tensor. The left-stretch tensor representation is preferred because it can be calculated without knowing $\mathbf{R}$. The stretch tensor is usually decomposed into its principal form

$$\mathbf{V} = \mathbf{T}\Lambda_{\mathbf{V}}\mathbf{T}^{\mathrm{T}}, \tag{12}$$

where $\mathbf{T}$ is the transformation matrix with column vectors that correspond to the principal stretch axes in the sample coordinate frame. The superscript T indicates the matrix transpose. The tensor $\Lambda_{\mathbf{V}}$ is diagonalized, with the principal stretches S_X, S_Y, and S_Z on the diagonal and zeros elsewhere. The Hencky tensor, $\mathbf{E}$, defined by

$$\mathbf{E} = \ln(\mathbf{V}) = \mathbf{T} \ln(\Lambda_{\mathbf{V}})\mathbf{T}^{\mathrm{T}}, \text{ and} \tag{13a}$$

$$\mathbf{V} = \exp(\mathbf{E}) = \mathbf{T}\exp(\Lambda_{\mathbf{E}})\mathbf{T}^{\mathrm{T}}, \tag{13b}$$

provides a better formulation for statistical estimation of the stretch tensor (Brandon, 1995; Mookerjee and Peek, 2014). Like the stretch tensor $\mathbf{V}$, the Hencky tensor is symmetric, which means that it has six unique values, as indicated by $\mathbf{E} = \mathbf{E}^{\mathrm{T}}$. The transformation matrix is the same for both $\mathbf{V}$ and $\mathbf{E}$. $\Lambda_{\mathbf{E}}$ is a diagonal matrix with the principal natural stretches E_X, E_Y, E_Z on the diagonal. Note that ln and exp in (13) refer to the matrix definitions for the natural logarithm and exponential functions (Higham, 2008 and as implemented in Matlab). The natural volume-strain is

$$E_V = \ln(V/V_0) = \mathrm{tr}(\mathbf{E}), \tag{14}$$

where V_0 and V are the initial and final volume of the sample, and tr is the trace (i.e. sum of the diagonal elements). The deviatoric Hencky tensor is defined by

$$\mathbf{E}' = \mathbf{E} - \mathbf{I}E_V/3, \tag{15}$$

where $\mathbf{I}$ is the identity matrix. Most methods of strain analysis do not provide information about the volume-strain component of the deformation (Brandon, 1995). This is also true for autocorrelation estimates of strain, given that we have no information about the length scale of the ACF for the material prior to deformation. In some cases, one can make independent estimates of volume strain (Wright and Platt, 1982; Ring and Brandon, 1999). Substitution of this information into (15) can be used to convert $\mathbf{E}'$ to $\mathbf{E}$.

We follow the usual convention where the principal values are organized as $E_X \geq E_Y \geq E_Z$, referring to the maximum extension direction X, the intermediate direction Y, and the maximum shortening direction Z.

The Hencky tensor extends the scalar concept of natural strain, $E = \ln(S)$, to a tensor representation, where stretch $S = l/l_0$ with l and l_0 representing the final and initial lengths of a material line. As proposed by Hencky (1931), natural strain scales linearly with strain rate during a finite deformation, so it provides a more natural representation of strain. In addition, natural strain also allows for a simpler representation of errors, as symmetric Gaussian variations around a mean value. In fact, the natural log is one of several power

transforms that are used in statistics to transform data sets into a form where standard Gaussian statistics can be used (Box and Cox, 1964).

For our purposes, we need to estimate the change in the lag vector from its present deformed state to its initial undeformed state. The ACF is assumed to have been isotropic in the initial state, so we only need the magnitude r_0 of the initial lag vector $r_0 = \|\mathbf{r}_0\|$. We define an "undeforming" function f_u (c.f. Spencer, 1980, eq. 6.21),

$$r_0 = f_u(\mathbf{r}; \mathbf{E}') = \sqrt{\mathbf{r}^{\mathrm{T}}\mathbf{V}'^{-2}\mathbf{r}} = \sqrt{\mathbf{r}^{\mathrm{T}}\exp(-2\mathbf{E}')\mathbf{r}}. \tag{16}$$

Note that in this equation and elsewhere below, we use a semicolon to separate known variables on the left (e.g., $\mathbf{r}$), from unknown parameters on the right (e.g., $\mathbf{E}'$).

6.1. Estimating the initial autocorrelation function

Autocorrelation is limited to the range -1 to $+1$, which makes the variable poorly suited for statistical analysis. The Fisher transform $\zeta = \mathrm{arctanh}(\rho)$ and its inverse $\rho = \tanh(\zeta)$ link the autocorrelation variable ρ to a new variable ζ, which has a range $-\infty$ to $+\infty$. This variable ζ usually follows a Gaussian distribution (Alexander, 1997), which makes it better suited for least-squares estimation, including calculation of uncertainties for the estimated parameters.

We seek a least-squares estimate for the unknown parameters $\mathbf{E}'$ and $\boldsymbol{c}$. We have already introduced $\mathbf{E}'$ above, which contains 6 unique coefficients. The vector $\boldsymbol{c}$ contains coefficients for a spline, which is used to represent the isotropic ACF as a function of r_0, as represented by $\zeta_0 = \zeta_0(r_0; \boldsymbol{c})$. We have experimented with several types of functional forms for ζ_0, but we found that a cubic spline is both sufficiently flexible to represent the isotropic ACF for all of our test cases and computationally fast, as needed for a nonlinear search algorithm. We would prefer to use the two-component model (5) but it is computationally too slow for our estimation here. The two-component model is used afterward to find best-fit estimates for the undeformed ACF.

For our least-squares calculation, we convert the gridded problem above into a serial list of $i = 1$ to n model equations

$$\zeta_i = \zeta_{0,i}(f_u(\mathbf{r}_i; \mathbf{E}'); \boldsymbol{c}) + \varepsilon_i \tag{17}$$

where $n = N_x N_y N_z$. Equation (17) shows that we are using the estimated isotropic ACF, along with the undeformed length of $\mathbf{r}$, to get predicted autocorrelation values. ε_i is a stochastic variable, and represents errors associated with the autocorrelation measurement. ε_i is assumed to be independently and identically distributed, with an expected mean of zero, and a variance of σ_ε^2.

The best-fit estimates $\widehat{\mathbf{E}}'$ and $\widehat{\boldsymbol{c}}$ are found numerically by searching for a candidate solution that minimizes the objective function,

$$\tilde{S} = S\left(\tilde{\mathbf{E}}', \tilde{\boldsymbol{c}}\right) = \frac{1}{\nu} \sum_{i=1}^{n} \left[\zeta(\mathbf{r}_i) - \zeta_0\left(f_u\left(\mathbf{r}_i; \tilde{\mathbf{E}}'\right); \tilde{\boldsymbol{c}}\right)\right]^2 \tag{18}$$

The tilde and caret symbols are used to indicate the state of estimation for a parameter variable. The tilde indicates a candidate estimate in the search, and the caret indicates a best-fit estimate that minimizes the least-squares objective function.

The degrees of freedom, ν, for the objective function is defined by $\nu = n - m_{\boldsymbol{c}} - m_{\mathbf{E}}$, where $m_{\boldsymbol{c}}$ and $m_{\mathbf{E}}$ are the number of unknown parameters in $\boldsymbol{c}$ and $\mathbf{E}$. The best-fit solution provides an estimate for $\widehat{\sigma}_\varepsilon^2 = \widehat{S}$.

Equation (18) is a separable least-squares problem (Moler, 2008,

p 154), in that the piecewise-spline estimate has a linear least-squares solution and the strain-tensor estimate has a nonlinear least-squares solution. As a result, the nonlinear search is focused exclusively on estimating the strain tensor. We use the "fmincon" function in MATLAB to estimate the six coefficients of the Hencky tensor

$$\mathbf{E}' = \begin{bmatrix} E'_{11} & E'_{12} & E'_{13} \\ E'_{12} & E'_{22} & E'_{23} \\ E'_{13} & E'_{23} & E'_{33} \end{bmatrix}, \tag{19}$$

subject to the constraint $tr(\mathbf{E}') = E'_{11} + E'_{22} + E'_{33} = 0$. Thus, the effective number of unknown coefficients for $\mathbf{E}'$ is $m_{\mathbf{E}} = 5$ for a 3D data set. Note that (15–19) are easily adapted to estimate a 2D strain tensor, which would have $m_{\mathbf{E}} = 2$.

Equation (18) is minimized in the following manner:

1) The search is started with a candidate solution $\tilde{\mathbf{E}}' = 0$, which corresponds to zero deformation.
2) Equation (16) and $\tilde{\mathbf{E}}'$ are used to convert the observed lag vectors $\mathbf{r}_i$ to a candidate estimate of their initial lag distances, $\tilde{r}_{0,i}$.
3) A candidate estimate for the initial isotropic autocorrelation function, $\zeta_0(f_u(\mathbf{r}_i; \tilde{\mathbf{E}}'); \tilde{\mathbf{c}})$, is estimated using a spline as a model function with $\tilde{r}_{0,i}$ and ζ_i.
4) The objective function (18) is evaluated using the candidate estimate $\zeta_0(f(\mathbf{r}_i; \tilde{\mathbf{E}}'); \tilde{\mathbf{c}})$.
5) The value of the objective function for the candidate estimates, $\tilde{S}(\tilde{\mathbf{E}}', \tilde{\mathbf{c}})$, is passed to the nonlinear search-algorithm, which tests for convergence to a final minimum value for $\tilde{S}$. If the test is positive, $\tilde{S}$ is returned as the best-fit estimate, $\widehat{S}$, and the routine also returns the best-fit estimates for the parameters, $\widehat{\mathbf{E}}'$ and $\widehat{\mathbf{c}}$. If the test is negative, then the algorithm selects a new candidate estimate for $\tilde{\mathbf{E}}'$ and returns to step 2 to evaluate that estimate.

With any nonlinear problem, there is always a concern that the optimization will become trapped in a local minimum, resulting in a flawed estimate. Our algorithm shows no sign of this kind of problem. Perhaps most telling is that the optimization gives estimates that fit our different datasets very well. Thus, we suspect that the objective function has a well-defined global minimum near the starting point $\tilde{\mathbf{E}}' = 0$. Bootstrap experiments, discussed below, indicate that the objective function has a quasi-Gaussian form around the best-fit minimum. There may be future cases where the solution fails, but this should be easy to spot by a poor fit between the best-fit objective function and data, or by wild, non-physical estimates for the parameters and their uncertainties.

6.2. Assessment of fit

The quality of fit can also be judged using a residuals plot, where the standardized residuals $\varepsilon_i/\sigma_\varepsilon$ are plotted on the y-axis and the estimated initial lag distance $r_{0,i}$, on the x-axis. The standardized residuals should be independently and identically distributed with a mean of zero and a standard deviation of one.

Another useful measure of the fit is the R^2 statistic, which is defined using the conventional formula

$$R^2 = 1 - \frac{\text{var}(\varepsilon_i)}{\text{var}(\zeta_i)}, \tag{20}$$

where ζ_i refers to the observed Fisher-transformed autocorrelation values.

The statistical independence of the residuals is tested using the Durbin–Watson statistic d (p. 68, Draper and Smith, 1998),

$$d = \frac{\sum_{j=2}^{n} (\varepsilon_i - \varepsilon_{j-1})^2}{\sum_{j=2}^{n} \varepsilon_j^2} \tag{21}$$

where the subscript j indicates the residuals in order of increasing r_0. The null case, where there is no serial correlation, has an expectation $d = 2$.

6.3. Uncertainties for estimated strain parameters

At termination, the MATLAB function "fmincon" reports the Hessian matrix $\mathbf{H}$ for the best-fit solution $\mathbf{E}'$. The Hessian is used to derive a linear approximation to the parameter covariance matrix (Press et al., 2007, p. 799–802)

$$\text{cov}(\text{vech}(\mathbf{E}')) \approx \sigma_\varepsilon^2 \mathbf{H}^{-1} \tag{22}$$

where the half-vectorization function, vech, converts $\mathbf{E}'$ into a six-component column vector for the strain parameters. As a result, $\text{cov}(\text{vech}(\mathbf{E}'))$ is a 6×6 covariance matrix for the six strain parameters in $\mathbf{E}'$.

For a nonlinear inverse, there is also a concern that approximated uncertainties may contain large errors. In a test, we found that uncertainties approximated by (22) agreed well with more accurate estimates determined by the bootstrap method (Efron, 1979). This result suggests that, near the best-fit solution, S has a quasi-linear relationship with respect to the parameters (Press et al., 2007, p. 807–818). We could use the bootstrap method to estimate all errors, but it is computationally expensive.

Given uncertainties for the coefficients in $\mathbf{E}'$, it is a simple matter to use the method of Hext (1963) to calculate uncertainties for the principal values and principal directions. This method has been used in the Yale STRAIN3D program since 1996, and works well for estimating uncertainties for strain analysis. The method is also widely used for statistical analysis of anisotropic magnetic susceptibility data (e.g., Hext, 1963; Jelinek, 1978; Owens, 2000).

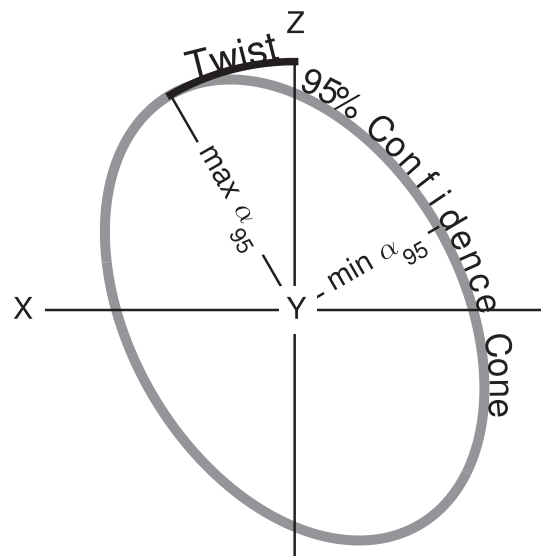We report 95 percent confidence intervals for both the

Fig. 8. The uncertainty for a best-fit principal direction is represented by an elliptical cone (gray line) that intersects the plane normal to the direction. The radii of the cone are given by max α_{95} and min α_{95}, and the orientation in the plane is given by the twist. This example shows the elliptical cone for the Y principal direction. Positive X and Z directions are shown for a right-handed coordinate system where Y points out of the image.

estimated magnitudes and directions for the principal strains, and the isotropy test of Hext (1963), which tests if the principal strains are significantly different from each other. The uncertainty for a best-fit principal direction is represented by an elliptical cone that defines the 95 percent confidence limit for the estimated principal direction (Fig. 8). The orientation of each elliptical cone is reported as the twist, which is the azimuth of the long axis of the cone in the plane normal to the best-fit principal direction. Keep in mind that principal directions are orthogonal. So given a best-fit principal direction, the twist is defined by the azimuth from the second principal direction to the third principal direction. The order of the directions is defined by the repeating sequence $+X$, $+Y$, and $+Z$, which are positive axes in a right-handed coordinate frame. For example, a twist of $+10°$ for the long-axis of the α_{95} elliptical cone around the best-fit estimate for the Y principal-strain direction would lie at $10°$ from the $+Z$ direction towards the $+X$ direction (Fig. 8). For most cases, the twist is 0 or $90°$, which indicates that the elliptical cone is aligned with the second and third principal directions.

7. Strain estimation examples

To demonstrate the advantages and limitations of our method, we find the best-fit strain parameters for several examples. The first set of examples, called "phantoms" (e.g., Shepp and Logan, 1974; Ketcham, 2005b), are synthetic cases where numerical calculations are used to generate an isotropic aggregate of spherical grains, which is then subjected to a known homogeneous deformation. The second set of examples illustrates estimation for naturally deformed rocks.

7.1. 3D synthetic (phantom) material

A 3D isotropic aggregate of spherical grains was generated using an event-driven, molecular-dynamics sphere-packing code (Lubachevsky and Stillinger, 1990; Donev et al., 2005a, 2005b; Skoge et al., 2006; available at http://cherrypit.princeton.edu/donev/Packing/PackLSD/Instructions.html). The code begins with a set of randomly distributed spheres, each with an initial velocity. The spheres interact with each other through collisions. The diameters of the spheres grow linearly in time until the number of collisions diverges and the diameters of spheres can no longer increase (see Donev, 2006 for an excellent introduction to these algorithms). These simulations are routinely used to study packing and flow in granular materials, (e.g., Torquato, 2002; Luding, 2004). This method generates aggregates that have the dense packing typical of geologic aggregates. The algorithms can also be used to create phantom materials with multiple grain sizes (Kansal et al., 2002; Donev et al., 2005a, 2005b), and non-spherical grain shapes (Donev et al., 2005a, 2005b).

The phantom contains 1200 non-overlapping grains that are packed to an average porosity of 50 percent (Fig. 9a). Prior to deformation, the grains were identical spheres, with a radius equal to 10 voxels. The phantom was deformed coaxially with principal stretches $S_X = 2$, $S_Y = 1$, and $S_Z = 0.5$. The X direction was rotated $30°$ from the sample x-axis toward the sample y-axis and the Z direction was aligned with the sample z-axes. The ACF for the deformed phantom is anisotropic, which causes a large spread in ζ, especially at $r/R < 1.5$ (Fig. 9b). Once the deformation is removed using the estimated best-fit strain parameters, the ACF collapses down to a single curve (Fig. 9c). The best-fit parameters agree well with those for the known deformation (Table 1). Note that the estimated grain radius, $R_S = 97$ μm, matches well with the known grain radius, 100 μm. The standardized residuals show some structure, but otherwise appear to be fairly uniform with increasing r_0/R (Fig. 9d).

The Durbin–Watson test indicates $d = 1.97$, which is consistent with our assumption that the residuals are independent.

Table 1 shows estimated deviatoric principal strains in terms of both stretches S and natural strains E, which are reported in centi-Neper (cNp). The Neper is the unit of measure for the natural-log scale (Mills, 1995), in the same sense that the Bel is the unit of measure for the base-10 log scale. A cNp is therefore equal to one hundredth of a natural strain unit, in the same way that a dB is equal to one tenth of a Bel. This scaling is convenient because, for small natural strains, in the range -15 cNp $< E < +15$ cNp, the cNp designation is approximately equal to percent elongation ($100 \, \Delta l/l_0$). This relationship results from the small-value approximation for the natural log, $\ln(1 + \varepsilon) \approx \varepsilon$ for $|\varepsilon| \ll 1$.

The confidence intervals for the stretches become asymmetric as the stretch deviates from 1, whereas the natural log confidence intervals remain symmetric in all cases. We have shown above that the Hencky tensor, which is the tensor representation of the natural strain, provides a compact notation relating tensor properties to strain invariants (e.g., E_D and E_V in Brandon, 1995). Likewise, the natural strains provide a simpler basis for estimating and reporting uncertainties.

7.2. 2D image of undeformed oolite

Our first natural example is a 2D photomicrograph of undeformed ooids from the Jurassic Stump formation in Wyoming (Fig. 10; Crespi, 1986). The image is more complicated than our previous examples, in that the ooids have internal structure and varying sizes. The Ramsay effect for this image is visible in the initial decay of the ACF. The Fry effect is small for three reasons. First, the ooids are anticlustered (e.g., Fig. 4d), but they are otherwise randomly distributed. Second, the size variation of the ooids reduces the Fry effect (Erslev, 1988). Third, resolution of the Fry effect requires averaging over a much larger set of ooids (Crespi, 1986), and thus would require a larger image.

For this example, the strain estimates given by the ACF method (Table 1) agree with those from the R_f/ϕ method, which was calculated using outlines for 42 ooids and the R_f/ϕ estimation algorithm of Shimamoto and Ikeda (1976). Note that for the 2D examples in Table 1, strains are reported as plane-strain deviatoric values given that we have no information about volume strain or the out-of-plane strain. The high value of R^2 indicates the best-fit solution fits the data very well. The Durbin–Watson test indicates no significant serial correlation. The residuals plot (Fig. 9d) shows some structure, but this is not unexpected given that autocorrelation estimates tend to retain some serial correlation (Priestley, 1981; Broersen, 2006).

7.3. 2D image of deformed oolite

A second photomicrograph example (Fig. 11a) shows deformed ironstone ooids (figure 7.7 in Ramsay and Huber, 1983). This sample is interesting because the ooid cores were deformed by an intra-crystalline mechanism, whereas the rims show truncations and fiber overgrowths, consistent with pressure solution. Ramsay and Huber (1983) used the R_f/ϕ and "Nearest Neighbor" methods to estimate the within-ooid strain and the bulk strain, respectively. The R_f/ϕ results were determined by us (Table 1), using digitized outlines of laminae from the core of the ooids, where they are not truncated by dissolution. The estimates are virtually identical to those from Ramsay and Huber (1983, p. 120, axial ratio = 1.22). The "Nearest Neighbor" estimate is based on Fig. 7.18 from Ramsay and Huber (1983). All three methods give the same principal directions. The ACF and R_f/ϕ estimates are essentially identical (Table 1). The reason is that the ACF is weighted towards the high-contrast ooid
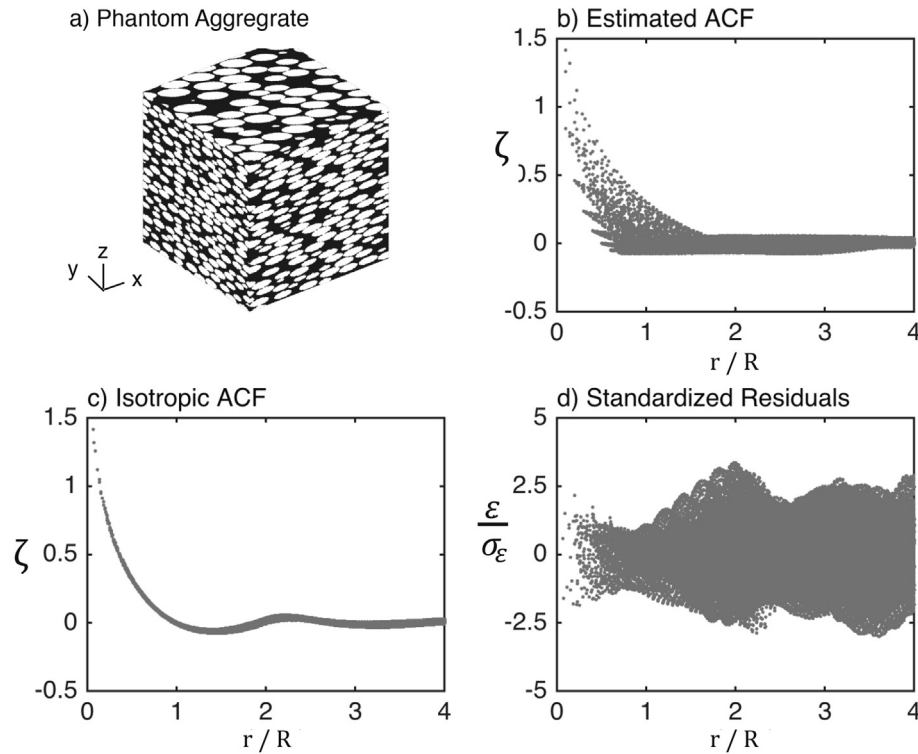
Fig. 9. Synthetic example (phantom) used to test the ACF method for estimating 3D strain. (a) A 3D rendering of the phantom, which was constructed from identical non-overlapping spheres and then deformed homogenously. (b) Observed ACF in the deformed coordinate frame with lag normalized to the radius R of the undeformed spheres. (c) Isotropic ACF, determined by removing estimated strain. (d) Standardized residuals for the best-fit isotropic ACF as a function of lag.

Table 1
Best-fit results for phantom, ooid, and Mg—Zr alloy samples.

Sample, method		Principal magnitudes and directions							Isotropy Prob. (%)	Grain radius R_S (μm)	Fit	
	Princ. Axis	S' (l/l_0)	E' (cNp)	Tr/Pl (deg)	max α_{95} (deg)	min α_{95} (deg)	Twist (deg)				R^2	d
Phantom												
Fig. 9 ACF	X	2.00 (0)	+69.21(5)	330/00	0.0	0.0	01	Y-Z: 0				
	Y	1.00 (0)	−00.36(4)	060/00	0.0	0.0	03	X-Z: 0	97[a]	0.96	1.97
	Z	0.50 (0)	−68.85(4)	234/90	0.0	0.0	90	X-Y: 0				
Undeformed Oolite												
Fig. 10 ACF	X	1.02 (0)	+02.12(8)	121/00	0.9	0.0	90	Y-Z: 0	96	0.93	1.99
	Z	0.98 (0)	−02.12(8)	031/00	0.9	0.0	00	X-Y: 0				
R_f/ϕ	X	1.00(2)	+1(1)	098/00	21	57	—	—	—	—	—
	Z	1.00 (2)	−1(1)	008/00	21	77						
Deformed Oolite												
Fig. 11 ACF	X	1.13 (0)	+12.2(1)	020/00	0.3	0.0	90	Y-Z: 0	828	0.94	1.97
	Z	0.89 (0)	−12.2(1)	110/00	0.3	0.0	00	X-Y: 0				
R_f/ϕ	X	1.09 (3)	+8(1)	020/00	3	3	—	—	—	—	—
inside grain	Z	0.92 (3)	−8(1)	110/00	3	3						
Nearest Neighbor	X	1.34	+29.11	025/00	—	—	—	—	—	—	—
	Z	0.75	−29.11	115/00								
Mg—Zr Alloy												
Fig. 15 ACF	X	2.41 (0)	+87.8(5)	090/00	0.1	0.0	90	Y-Z: 0	21	0.94	1.41
	Z	0.42 (0)	−87.8(5)	180/00	0.1	0.0	00	X-Y: 0				
Mg—Zr Alloy, segmented												
Fig. 16 ACF	X	1.18 (0)	+16.1(1)	080/00	0.2	0.0	90	Y-Z: 0	20	0.99	1.84
	Z	0.85 (0)	−16.1(1)	170/00	0.2	0.0	00	X-Y: 0				

Errors are reported using concise notation. For example 1.4(3) = 1.4 ± 0.3.
Orientations are reported in sample coordinates.
[a] Initial grain radius for the Phantom example was scaled to 100 microns for this calculation.

cores. The "Nearest Neighbor" estimate shows more strain, but this is expected given the deformation between the grains, including dissolution and overgrowths.

The ACF method works best where each grain has a relatively uniform intensity. The concentric rings in the ooids could cause

problems. The ACF is influenced by this within-grain structure, which might cause the ACF method to give biased strain estimates (Fig. 12). The 2D image in Fig. 12 was constructed by drawing two circular rings and then deforming the rings to a strain ratio $S_X/S_Z = 2$. At small lags, the ACF contours for this image have simple
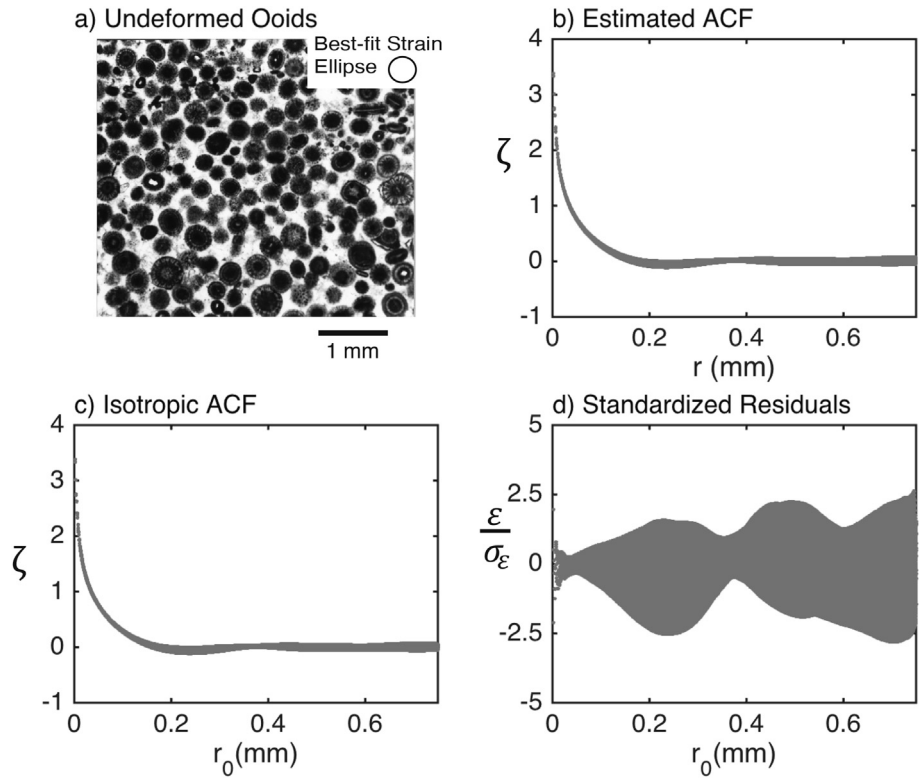
Fig. 10. Use of ACF method to estimate strain for (a) 2D photomicrograph of undeformed ooids from the Jurassic Stump formation in Wyoming (Crespi, 1986). See caption in Fig. 9 for details of (b−d), and Table 1 for results.
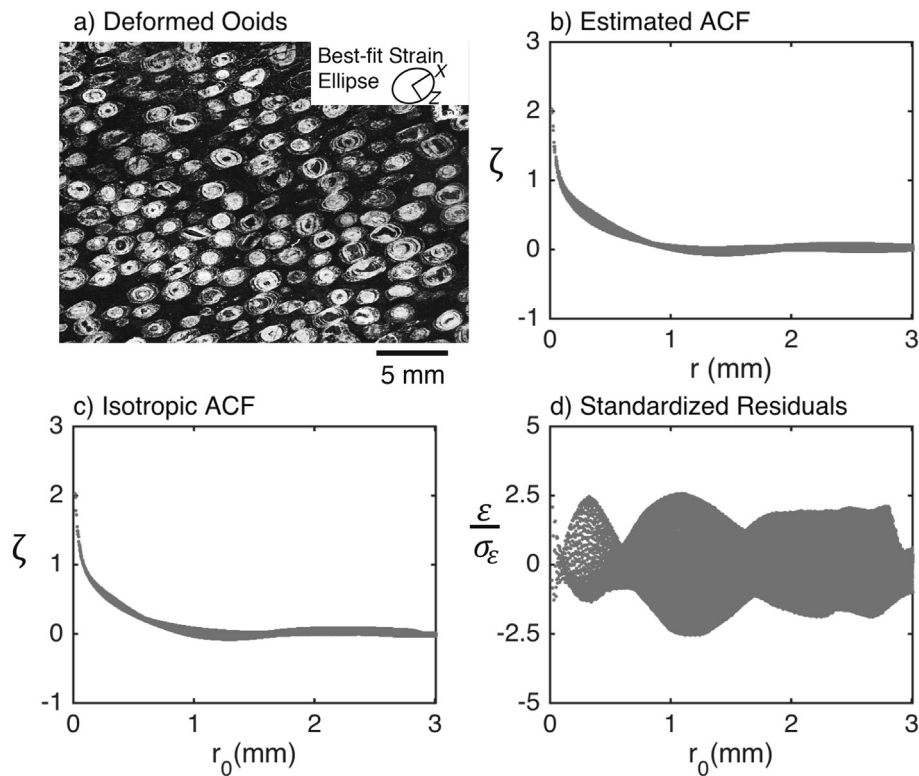

Fig. 11. Use of ACF method to estimate strain for (a) 2D photomicrograph of deformed ooids (figure 7.7 in Ramsay and Huber, 1983). See caption in Fig. 9 for details of (b−d), and Table 1 for results.
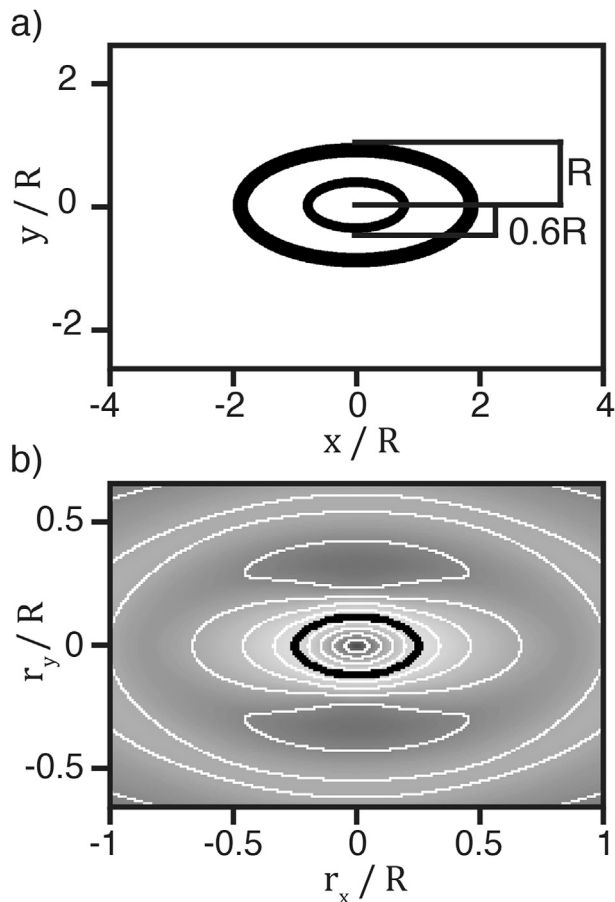
a)

b)

Fig. 12. The effect of internal particle structure on the ACF. (a) A test object composed of concentric rings with the same aspect ratio. (b) The ACF contours are not everywhere elliptical, but instead have "hot-dog" shapes at intermediate lags. The black line is r^*.

elliptical shapes, but, at larger lags, the contours take on "hot dog" shapes caused by smearing in the X direction. The smearing results from correlation between the different rings, which produces an upward bias in the strain ratio $S_X/S_Z = 2.1$, as estimated using the ACF method. At larger lags, the correlation between the different rings is reduced, and the contour shape is more elliptical.

7.4. 3D tomograms of pressure-solved sandstones

We now consider X-ray attenuation tomograms for a pressure-solved sandstone from the Olympic Subduction Complex in Washington State (Brandon et al., 1998). Sample 92810-3 is from the Grand Valley Assemblage (Tabor and Cady, 1978) and was deformed along a path that reached a maximum depth of about 12 km and a maximum temperature of 250° C at about 18 Ma (Brandon et al., 1998). The microstructure of the sample is typical of pressure-solved sandstones from this and other subduction complexes (Tabor and Cady, 1978; Feehan and Brandon, 1999; Ring and Brandon, 1999; Ring et al., 2001; Rahl et al., 2011).

The tomogram (Fig. 13) was acquired at the X-ray computed tomography facilities at the Advanced Photon Source at Argonne National Labs (Beamline 13-BM-D). The voxels are cubes, measuring 7.54 μm on each side. The sample is approximately $3 \times 3 \times 10$ mm, with X approximately aligned with the long dimension of the sample. The X-ray attenuation is shown by the grayscale, increasing from black to white.

The sandstone is a turbidite and is dominated by angular, first-cycle volcanic detritus. The tomogram shows features related to both the composition of the sandstone and the fabrics resulting from the pressure-solution deformation (Fig. 14). As a reminder, X-ray attenuation increases with grain density and mean atomic number. In particular, minerals with high concentrations of Fe, Mg, Ti and Zr are bright (high attenuation). For this sample, the white grains correspond to pyrite, magnetite and zircon; the intermediate grains, to lithic rock fragments; and the dark grains, to quartz and plagioclase.

The tomogram also resolves fabrics related to the pressure-solution deformation. Bright values on grain margins and selvages are related to residual concentrations of insoluble phases, such as Fe—Ti oxides and phyllosilicates. The fiber overgrowths are dominated by quartz and white mica, and have a fairly uniform appearance when viewed in thin section, despite the heterogeneous assortment of detrital grains. In the tomogram, the overgrowths also have a uniform appearance throughout the volume. They everywhere seem to have a higher X-ray attenuation than quartz, which might be due to the higher atomic number of potassium in the white mica.

Thin section observations indicate that the shortening was accommodated by localized dissolution between grains, and extension, by the precipitation of directed overgrowths. Grain interiors are generally undeformed. The fiber overgrowths mantle the grains in the X direction and are unidirectionally aligned with that direction. From these observations we conclude that the initial dimensions of the grains are preserved in the X direction. This conclusion holds for many pressure-solved sandstones (Feehan and Brandon, 1999; Ring and Brandon, 1999; Ring et al., 2001; Rahl et al., 2011).

Some care is needed to account for this heterogenous intergranular deformation. We find it useful to identify how these different components of the deformation affect the bulk principal stretches. The change in grain shape, as caused by dissolution, is represented by principal stretches S_{gX}, S_{gY}, and S_{gZ}. The contribution of fiber overgrowth is represented by principal stretches S_{fX}, S_{fY}, and S_{fZ}. The principal stretches for the bulk deformation are given by $S_X = S_{gX} S_{fX}$, $S_Y = S_{gY} S_{fY}$, and $S_Z = S_{gZ} S_{fZ}$.

Considering that the grains have uniform interiors that compose a large fraction of the image, our interpretation is that the ACF method provides estimates of the change in grain dimensions (Table 2). The thin section evidence indicates that the grain dimensions remain unchanged in the X direction, so $S_{gX} = 1$. As a result, the other principal strains for the grain shape are $S_{gY} = 0.97$ and $S_{gX} = 0.52$. The volume stretch for the grains is $S_{gV} = S_{gX} S_{gY} S_{gZ}$, which for this sample is $S_{gV} \approx 0.51$, or about 50% loss of grain volume.

For comparison, we also used the PDS method to measure grain stretches (Table 2). PDS measurements are based on microscopy measurements made in 2D thin sections, but they are corrected to account for stereological effects associated with 2D sections through 3D volumes (Rahl et al., 2011). The PDS method indicates $S_{gV} \approx 0.76$. The ACF method has the advantage that it provides a full estimate in 3D, but is less sensitive to the actual dimensions of the grains.

We consider now the bulk deformation of this sample, S_X, S_Y and S_Z. Modal measurements indicate that fiber overgrowth composes 15 percent of the sample. For unidirectional fibers, the fiber-related stretch in the X direction is $S_{fX} = 1/(1 - m)$, where m is the modal fraction of overgrowth (Feehan and Brandon, 1999). The bulk strain in the Y and Z directions is limited to dissolution of the grain boundaries, so $S_{fY} = S_{fZ} = 1$. Using the ACF results and the equations above for fiber and grain strains, we estimate that the bulk strain in this sample caused by pressure solution is $S_X = 1.17$, $S_Y = 0.97$, and
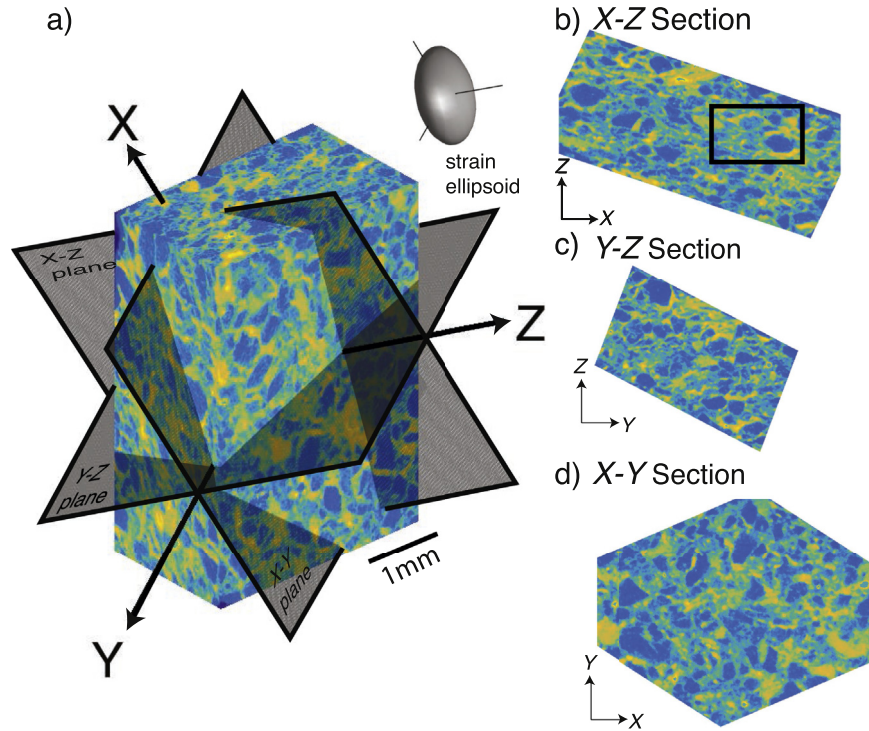
Fig. 13. Tomogram for deformed sandstone (sample 92810-3 from the Olympic subduction complex). (a) 3D rendering showing principal strain axes and sections as determined using the ACF method. (b–d) Slices through the tomogram along principal strain sections. See Table 2 for results. The black box in panel (b) outlines the region shown in Fig. 14.
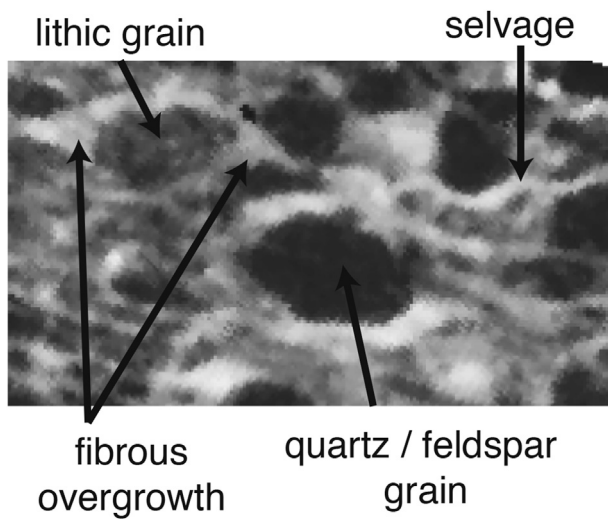

Fig. 14. Pressure-solution fabric elements in *X-Z* slice of sample 92810-3 tomogram. Arrows indicate quartz/feldspar and lithic grains, fibrous overgrowths, and selvages. The magnified view is outlined by the black box in Fig. 13b.

$S_Z = 0.52$, with a volume stretch of $S_V = 0.59$. In other words, the pressure-solution deformation generated a net 41% volume loss from the bulk sample. Note that this analysis does not account for deformation associated with compaction of the sandstone, as selvage and overgrowth fabrics indicate that the sandstone had little porosity when pressure solution started (see Feehan and Brandon, 1999 for further discussion of this issue).

The initial grain size is estimated by fitting the two-component model in (5) to the estimated isotropic ACF, and by scaling the measurement to account for the absence of intragranular deformation in the *X* direction. The estimated average grain radius is

149 μm (Table 2).

7.5. 2D image of deformed Mg–Zr alloy

Images and tomograms may also contain features that are unrelated to the deformation of the sample, so care is required for proper interpretation of results. We discuss here an example that illustrates this point.

Fig. 15a shows a hydrided Mg–Zr alloy with minor Zr grains (Harris, 1973). Such materials are commonly used in nuclear reactors due to their resistance to creep at high temperatures (e.g., Wadsworth et al., 2002). The original fabric was formed by inducing growth of Zr precipitates within the metal, and then passing the alloy through rollers, which produces a flattening fabric. Later, the alloy was subjected to a uniaxial extension, with *X* oriented in the image vertical. The important point is that the laminated fabric predates the extensional fabric. The alloy accommodated about half of the extension by dilational "veins" or overgrowths, and the other half by microfaulting of the rolled fabric. The overgrowth regions are called "denuded zones" because they lack the Zr precipitates that were in the original alloy. The fabric at present appears granular, but the granular structure is actually defined by microfaults.

The modal abundance of the denuded zones is 4.6 percent (Harris, 1973), which accommodated 4.6 cNp of extension in the vertical. Harris (1973) suggested the denuded zones formed by mass transfer associated with Nabarro-Herring creep (see Xu et al., 2015, for an alternative interpretation), which implies that the "grains" have internal deformation as well. The ACF method correctly estimated the principal strain directions, but failed to correctly estimate the principal strains (Table 1). This result is not surprising given that the laminar fabric has nothing to do with the extensional deformation. One might speculate that the estimated principal strains are representative of the full deformational history

Table 2
Best-fit results for pressure-solved sandstone sample.

Sample, method		Principal magnitudes and directions							Isotropy Prob. (%)	Grain radius R_S (μm)	Fit	
	Princ. Axis	S_g (l/l₀)	E_g (cNp)	Tr/Pl (deg)	max α_{95} (deg)	min α_{95} (deg)	Twist (deg)				R^2	d
92810-3												
Fig. 13	ACF	X	1.00 (0)	+00.00(5)	263/09	0.8	0.0	00	Y-Z: 0			
		Y	0.97 (0)	−02.68(5)	169/20	0.8	0.0	00	X-Z: 0	120	0.97	1.97
		Z	0.52 (0)	−64.91(5)	016/68	0.0	0.0	84	X-Y: 0			
		V	0.51 (0)	−67.59(9)	−	−	−	−	−			
	PDS	X	1.00 (0)	+00(0)	263/09	14	14					
		Y	1.00 (10)	+00(10)	169/20	14	14		−	−	−	−	−
		Z	0.76 (8)	−27(10)	016/68	14	14					
		V	0.76 (10)	−27(13)	−	−	−					

S_{gX} is set to 1 because grains have not deformed internally in the X direction.
Errors are reported using concise notation. For example 1.4(3) = 1.4 ± 0.3.
Orientations are reported in geographic coordinates.
PDS measurements and errors are calculated according to Feehan and Brandon (1999) and 3D correction introduced by Rahl et al. (2011).

of the alloy, including rolling and stretching, but we have no way to test that idea.

Inspection of Fig. 15b shows that the deformed ACF field has a complicated rectilinear pattern, quite different from the simple ellipsoidal pattern seen in the previous examples. The ACF is clearly dominated by the Zr precipitates, which have a large contrast with the other features in the image. One can see that the ACF is not elliptical, which is an indication that the image is not suitable for strain estimation using the ACF method.

An alternative approach is to outline the "grains" and replace the laminated fabric inside each grain with a uniform and unique grayscale value (Fig. 16). The strain estimates for this example (Table 1) indicate that the "grains" are slightly elongate in the vertical, but the method overestimated the principal strains. The reason that this example fails to give useful strain estimates is that the "grains" are not passive markers, but instead were produced by microfaulting. The ACF analysis could be useful, in this case, for estimating the aspect ratio of fault-bounded domains, but it cannot be expected to provide information about strain magnitudes.

8. Discussion

In this paper, we started with schematic examples that help illustrate how the ACF might be used to estimate anisotropy and strain. This conceptual framework builds on the pioneering work of Panozzo Heilbronner (1992). Our main contributions are the introduction of a least-squares method for estimating anisotropy and strain from real images and tomograms, and a discussion of how different fabric features influence the ACF estimates. The examples in Tables 1 and 2 provide a useful test of the ACF method,
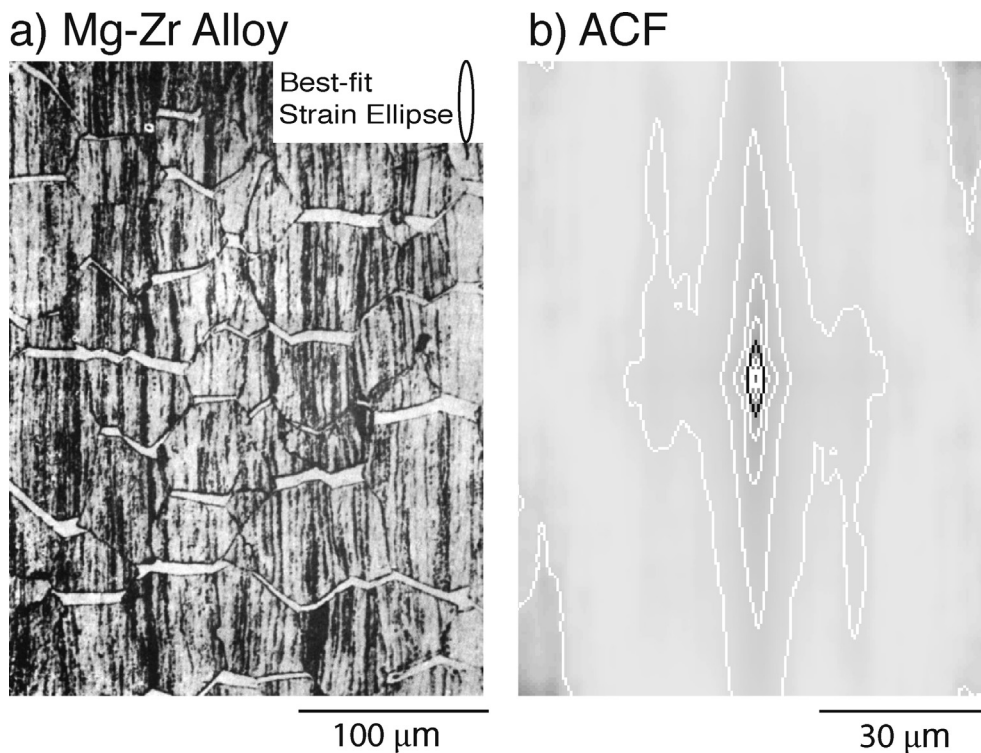

a) Mg-Zr Alloy

Best-fit Strain Ellipse

100 μm

b) ACF

30 μm

Fig. 15. A cautionary tale for using the ACF method. (a) Photomicrograph and (b) ACF of an Mg−Zr alloy that was initially formed by rolling, which produced the vertical laminar structure. The horizontal light gray zones in (a) are overgrowths that formed under high temperature conditions. During this deformation, the fabric was also broken into blocky domains by shear fractures. See Table 1 for results.
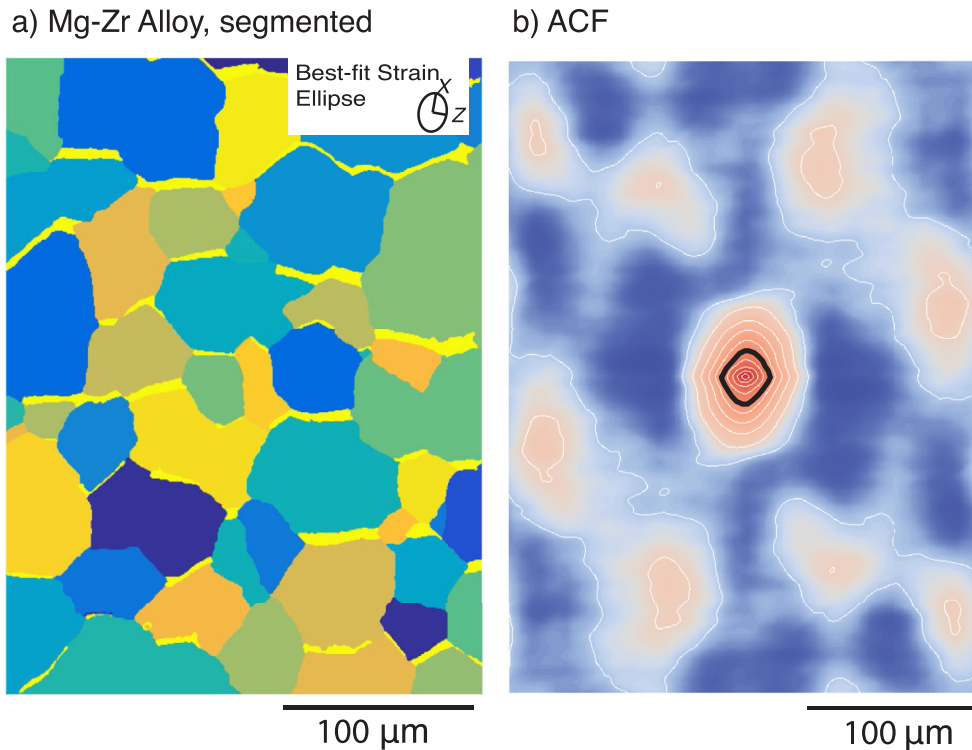
Fig. 16. Segmentation of the "grains" in the Mg–Zr alloy dramatically changes the best-fit strain results. (a) The "grains" are manually segmented and assigned uniform grayscale values. (b) The ACF suggests the segmented grains are elongated in the vertical direction. Black line marks the r_0^* contour. See Table 1 for results.

and illustrate some complex cases where the method might fail or special care is required to get useful results.

We finish here with a discussion of some general issues. The first concerns the interpretation of the least-squares uncertainties. The next are three issues for future development of the ACF method.

8.1. Estimated least-squares uncertainties

Many readers may be skeptical of the small estimated uncertainties reported for our ACF estimates (Tables 1 and 2). What is important to remember is that the reported uncertainties are only representative of the uncertainty associated with the least-squares estimate. The least-squares method not only estimates a best-fit model, but also the residuals, which are the estimated errors in the data relative to that model. The uncertainties in the parameters are simply a function of how the variation in the residuals translates into variation in the estimated values of the parameters.

There may be other sources of error beyond those represented by the residuals. For example, the model may be incorrectly specified. The best check for a well-fit model is by inspection of the results, such as the deformed ACF, the undeformed ACF, and the residuals relative to the estimated isotropic lag. The R^2 and Durbin–Watson statistics provide additional diagnostic clues.

Usually, it is obvious when the model function fails. The Mg–Zr alloy provides a useful example, in that the contours of the deformed ACF are far from elliptical. Thus, we should know, long before applying the ACF method, that the method will probably not work.

It might also be thought that heterogeneous strain at the grain scale may also invalidate the ACF results. The pressure-solved examples illustrate a common type of heterogeneous deformation, where the deformation is accommodated by dissolution and precipitation in different positions along grain boundaries. However,

we have shown that the method seems to work well for estimating grain strain in the pressure solution examples, because the grains are the dominant features of the fabric.

8.2. Symmetry of the ACF

Our strain estimates have orthorhombic symmetry, because the model function is based on the strain tensor, which cannot represent symmetry lower than orthorhombic. The ACF, however, only requires a center of symmetry, and thus can represent symmetries less than orthorhombic (Priestley, 1981; Panozzo Heilbronner, 1992). Therefore, we anticipate that the ACF method may be useful for studying low symmetry fabrics, such as those found in rocks from ductile shear zones. For example, the ellipticity of large porphyroblasts may be significantly different from small neoblasts or micas in the surrounding matrix. Panozzo Heilbronner (1992) provided examples of ACFs with lower than orthorhombic symmetry, and some suggestions for interpreting these fabrics, such as the sense of shearing.

8.3. ACF sensitivity

In our opinion, the most important next step for the ACF method is to characterize the sensitivity of the ACF for different fabric features. The intensity provides a clue as to what features will dominate. But as Fig. 6 demonstrates, the influence of fabric features at any particular ACF lag value is also dependent on the feature size and spacing. If the ellipses in Fig. 6 had similar intensity values, the ACF would find parameters that are some average of the anisotropy of the two elliptical phases. A method of adjusting intensity values in the image to focus the ACF estimates of strain on different fabric elements would be useful. For the Mg–Zr alloy (Figs. 15 and 16), segmenting the fault-bounded domains focused the ACF estimate

of anisotropy on the fault-bounded domains, rather than the foliated Zr streaks.

For 3D objects, manual segmentation of each slice is labor intensive, and computerized segmentation methods (e.g., Ketcham, 2005b) may be especially useful. In many images, however, there may be too much overlap in the intensity values of different fabric features to allow for precise segmentation. We found this to be the case for the pressure-solved sandstone (Fig. 13). These cases require a continuous adjustment to the intensity values to emphasize different features. One approach would be to manually adjust the intensity values in Photoshop using the gamma-correction tool. The same correction can be automated and applied to each "slice" in a stack of images that makeup a tomogram. Alternatively, a statistical approach can also be used to continuously rescale the intensity values (Eisemann et al., 2011).

8.4. Dynamic range and neighbor correlation

An additional objective is to allow for estimation of anisotropy as a function of lag. At present, the X-ray tomogram of the pressure-solved sandstone example has excellent resolution for estimating self-correlation, but it lacks the sample size and dynamic range to estimate neighbor-correlation.

To explain, let's consider first the requirements for minimum resolution. In our experience, the raw image should have a voxel size smaller than about 2.5 percent of the grain diameter. This value allows for "2×2 binning", as needed to remove aliasing errors (Rivers et al., 2010). As a result, the actual operational image should have a voxel size smaller than 5% of the grain diameter. For comparison, the tomogram for our pressure-solved sample has voxel sizes of 7.54 μm, which works out to ~3% of the grain diameter ($2R_S \approx 240$ μm). One might consider smaller voxels if there are fine features, such as overgrowths or selvages, that need to be identified for modal analysis or removed by image processing. Accurate modal analysis would require a voxel resolution of 1—5 μm.

What we are lacking at present is sufficient dynamic range, which would allow images of larger samples while maintaining local resolution. For example, our tomogram for the pressure-solved sandstone has an average of ~6 grain diameters across each dimension. This size is sufficient for determining self-correlation, but it is inadequate to fully resolve neighbor-correlation. For example, Crespi (1986) estimated that, for the Fry method in 2D, measurements of about 500—1000 grains are needed to get a successful solution. This works out to an image with an average of 22—32 grains across each dimension. Thus, the pressure-solved sandstone, which has an average grain diameter of ~220 μm, would require tomograms that are 5—8 mm in each dimension. The raw image, after binning, would have to be 880 to 1200 voxels per dimension. For comparison, each working dimension of our cropped tomograms is about 400—500 voxels.

X-ray tomography imaging can be divided into two types of setups: commercially available desktop scanners and custom-designed synchrotron facilities. Commercial scanners use X-ray tubes, in which a target, such as tungsten, is impacted by an electron beam to generate X-rays. For synchrotrons, electrons traveling at velocities near the speed of light are accelerated in storage rings using bending magnets, undulators, and wigglers. The electrons produce X-rays as they circle through the storage ring, and those X-rays are extracted at fixed points around the ring. The main difference between commercial and synchrotron scanners is that the synchrotron has a much larger photon flux spread over a larger range of X-ray energy (Fusseis et al., 2014). As a result, the X-ray beam can be filtered to specific energy bands while maintaining a large enough photon flux for tomography. Selecting a specific energy band is useful for avoiding beam-hardening artifacts, or

optimizing attenuation contrast. In addition, a large photon flux means that the tomogram can be acquired quickly, on the order of 10 min at present, and with low image noise. In contrast, the lower photon flux for commercial systems means acquisition times on the order of 1.5—4 h for similar sample sizes.

The voxel resolution and sample size requirements also differ between commercial and synchrotron systems. The Argonne APS Beamline 13-BM D can image a cylinder with a diameter less than 50 mm and a height less than 4 mm. The CCD in use during our measurements provided 650 pixels across the radial dimension after binning for aliasing. If we consider an 8 mm diameter cylinder, the voxel resolution would be about 12 μm (see Gualda and Rivers, 2006, for further details). Commercial systems are more flexible about sample size and can also provide voxel sizes down to the micron scale for small samples. But as noted above, the acquisition times are much longer.

The small sample size creates another problem, in that it is challenging to maintain a reference to the geographic orientation of the sample. Given our experiences, we recommend that samples be prepared as small cores, on the order of 8 mm in diameter, which is about the diameter of a pencil, and several cm in length. The azimuthal direction of the core could be marked with a scribe. Using this approach, the orientation of the core can then be directly acquired from the tomogram. For comparison, note that a rock chip for a standard thin-section billet is about 26 mm $\times$ 46 mm $\times$ 10 mm.

9. Conclusions

We have outlined the utility of the ACF method for estimating anisotropy and deformation. Our analyses here have emphasized thin-section images and X-ray tomograms, but clearly the ACF method can be applied to other kinds of field variables, such as composition and crystal orientation. In comparison to other methods of strain estimation, the ACF method allows for more precise representations of objects, and does not require fitting ellipses to objects or abstractions of grain boundaries. The method also works equally well for both 2D and 3D images.

The method works best for images or tomograms where grains have a uniform internal intensity but a strong contrast with the intensity of other grains and matrix. For example, a tomogram of a granite or a polymictic sandstone should work well, but a tomogram of a monomineralic rock, such as a limestone, dunite, or quartzite, would likely give poor results unless there are significant variations in attenuation between grains. It is also a challenge to work with grains that have complicated internal structure, as illustrated by the examples of the ironstone oolite and the Mg—Zr alloy. There are ways to treat these cases, such as manually segmenting grains, as was done for the metal example. In this regard, computerized segmentation methods (Ketcham, 2005b) may prove useful, especially for 3D tomograms. Right now, our analysis is weighted towards the self-correlation component of the ACF, and thus is most sensitive to particle shapes. Further work is needed to develop methods that would be able to provide separate estimates of the anisotropies associated with self-correlation and neighbor-correlation. The method could also be generalized to give a continuous estimate of anisotropy as a function of lag.

References

Alexander, T., 1997. Is AGN variability correlated with other AGN properties?—ZDCF analysis of small samples of sparse light curves. In: Maoz, D., Sternberg, A., Leibowitz, E.M. (Eds.), Astronomical Time Series. Springer, Netherlands, pp. 163–166.

Andrä, H., Combaret, N., Dvorkin, J., Glatt, E., Han, J., Kabel, M., Keehm, Y., Krzikalla, F., Lee, M., Madonna, C., Marsh, M., Mukerji, T., Saenger, E.H., Sain, R., Saxena, N., Ricker, S., Wiegmann, A., Zhan, X., 2013. Digital rock physics benchmarks—part I: imaging and segmentation. Comput. Geosci. 50, 25–32. http://dx.doi.org/10.1016/j.cageo.2012.09.005.

Baker, D.R., Mancini, L., Polacci, M., Higgins, M.D., Gualda, G.A.R., Hill, R.J., Rivers, M.L., 2012. An introduction to the application of X-ray microtomography to the three-dimensional study of igneous rocks. Lithos 148, 262–276. http://dx.doi.org/10.1016/j.lithos.2012.06.008.

Baveye, P.C., Laba, M., Otten, W., Bouckaert, L., Sterpaio, P.D., Gowami, R.R., Grinev, D., Houston, A., Hu, Y., Liu, J., Mooney, S., Pajor, R., Sleutel, S., Tarquis, A., Wang, W., Wei, Q., Sezgin, M., 2010. Observer-dependent variability of the thresholding step in the quantitative analysis of soil images and X-ray microtomography data. Geoderma 157, 51–63. http://dx.doi.org/10.1016/j.geoderma.2010.03.015.

Boone, M., Dewanckele, J., Boone, M., Cnudde, V., Silversmit, G., Van Ranst, E., Jacobs, P., Vincze, L., Van Hoorebeke, L., 2011. Three-dimensional phase separation and identification in granite. Geosphere 7 (1), 79–86. http://dx.doi.org/10.1130/GES00562.1.

Berger, M.J., Hubbell, J.H., Seltzer, S.M., Chang, J., Coursey, J.S., Sukumar, R., Zucker, D.S., Olsen, K., 2010. XCOM: Photon Cross Section Database (Version 1.5). National Institute of Standards and Technology, Gaithersburg, MD [Online] Available: http://physics.nist.gov/xcom.

Bevington, P.R., Robinson, D.K., 2003. Data Reduction and Error Analysis. McGraw–Hill, New York.

Box, G.E., Cox, D.R., 1964. An analysis of transformations. J. R. Stat. Soc. Ser. B Methodol. 211–252.

Brabant, L., Vlassenbroeck, J., De Witte, Y., Cnudde, V., Boone, M.N., Dewanckele, J., Van Hoorebeke, L., 2011. Three-dimensional analysis of high-resolution X-ray computed tomography data with Morpho+. Microsc. Microanal. 17 (02), 252–263. http://dx.doi.org/10.1017/S1431927610094389.

Brandon, M.T., 1995. Analysis of geologic strain data in strain-magnitude space. J. Struct. Geol. 17 (10), 1375–1385. http://dx.doi.org/10.1016/0191-8141(95)00032-9.

Brandon, M.T., Roden-Tice, M.K., Garver, J.I., 1998. Late Cenozoic exhumation of the cascadia accretionary wedge in the Olympic Mountains, northwest Washington State. Geol. Soc. Am. Bull. 110 (8), 985–1009. http://dx.doi.org/10.1130/0016-7606(1998)110<0985:LCEOTC>2.3.CO;2.

Broersen, P.M., 2006. Automatic Autocorrelation and Spectral Analysis. Springer, London.

Brun, F., Mancini, L., Kasae, P., Favretto, S., Dreossi, D., Tromba, G., 2010. Pore3D: a software library for quantitative analysis of porous media. Nucl. Instrum. Methods Phys. Res. Sect. A Accel. Spectrom. Detect. Assoc. Equip. 615 (3), 326–332. http://dx.doi.org/10.1016/j.nima.2010.02.063.

Buscombe, D., Rubin, D.M., Warrick, J.A., 2010. A universal approximation of grain size from images of noncohesive sediment. J. Geophys. Res. Earth Surface (2003–2012) 115 (F2).

Carlson, W.D., 2006. Three-dimensional imaging of earth and planetary materials. Earth Planet. Sci. Lett. 249 (3), 133–147. http://dx.doi.org/10.1016/j.epsl.2006.02.020.

Chantler, C.T., Olsen, K., Dragoset, R.A., Chang, J., Kishore, A.R., Kotochigova, S.A., Zucker, D.S., 2005. X-ray Form Factor, Attenuation and Scattering Tables (Version 2.1) [Online] Available: National Institute of Standards and Technology, Gaithersburg, MD http://physics.nist.gov/ffast.

Cnudde, V., Boone, M.N., 2013. High-resolution X-ray computed tomography in geosciences: a review of the current technology and applications. Earth-Sci. Rev. 123, 1–17. http://dx.doi.org/10.1016/j.earscirev.2013.04.003.

Crespi, J.M., 1986. Some guidelines for the practical application of Fry's method of strain analysis. J. Struct. Geol. 8 (7), 799–808. http://dx.doi.org/10.1016/0191-8141(86)90026-X.

Cule, D., Torquato, S., 1999. Generating random media from limited microstructural information via stochastic optimization. J. Appl. Phys. 86 (6), 3428–3437. http://dx.doi.org/10.1063/1.371225.

Debye, P., Bueche, A.M., 1949. Scattering by an inhomogeneous solid. J. Appl. Phys. 20 (6), 518–525.

Debye, P., Anderson Jr., H.R., Brumberger, H., 1957. Scattering by an inhomogeneous solid. II. The correlation function and its application. J. Appl. Phys. 28 (6), 679–683. http://dx.doi.org/10.1063/1.1722830.

Denison, C., Carlson, W.D., Ketcham, R.A., 1997. Three-dimensional quantitative textural analysis of metamorphic rocks using high-resolution computed X-ray tomography: part I. Methods and techniques. J. Metamorph. Geol. 15, 29–44. http://dx.doi.org/10.1111/j.1525-1314.1997.00006.x.

Denison, C., Carlson, W.D., 1997. Three-dimensional quantitative textural analysis of metamorphic rocks using high-resolution computed X-ray tomography: part II. Application to natural samples. J. Metamorph. Geol. 15, 45–57. http://dx.doi.org/10.1111/j.1525-1314.1997.00007.x.

Donev, A., Torquato, S., Stillinger, F.H., 2005a. Neighbor list collision-driven molecular dynamics simulation for nonspherical hard particles. I. Algorithmic details. J. Comput. Phys. 202 (2), 737–764. http://dx.doi.org/10.1016/j.jcp.2004.08.014.

Donev, A., Torquato, S., Stillinger, F.H., 2005b. Neighbor list collision-driven molecular dynamics simulation for nonspherical hard particles. II. Applications to ellipses and ellipsoids. J. Comput. Phys. 202 (2), 765–793.

Donev, A., 2006. Jammed Packings of Hard Particles (Ph.D. thesis). Princeton University.

Draper, N.R., Smith, H., 1998. Applied Regression Analysis, third ed. Wiley-Interscience, New York, ISBN 0-471-17082-8.

Ebel, D.S., Rivers, M.L., 2007. Meteorite 3-D synchrotron microtomography: methods and applications. Meteorit. Planet. Sci. 42, 1627–1646. http://dx.doi.org/10.1111/j.1945-5100.2007.tb00595.x.

Eisemann, M., Albuquerque, G., Magnor, M., 2011. Data driven color mapping. In: Proceedings of EuroVA: International Workshop on Visual Analytics, Bergen, Norway.

Elangovan, P., Hezel, D.C., Howard, L., Armstrong, R., Abel, R.L., 2012. PhaseQuant: a tool for quantifying tomographic data sets of geological specimens. Comput. Geosci. 48, 323–329. http://dx.doi.org/10.1016/j.cageo.2012.01.014.

Efron, B., 1979. Bootstrap methods: another look at the jackknife. Ann. Stat. 7, 1–26.

Erslev, E.A., 1988. Normalized center-to-center strain analysis of packed aggregates. J. Struct. Geol. 10 (2), 201–209. http://dx.doi.org/10.1016/0191-8141(88)90117-9.

Feehan, J.G., Brandon, M.T., 1999. Contribution of ductile flow to exhumation of low-temperature, high-pressure metamorphic rocks: San Juan-Cascade nappes, NW Washington State. J. Geophys. Res. 104 (B5), 10883–10902. http://dx.doi.org/10.1029/1998JB900054.

Friese, K.I., Cichy, S.B., Wolter, F.E., Botcharnikov, R.E., 2013. Analysis of tomographic mineralogical data using YaDiV—overview and practical case study. Comput. Geosci. 56, 92–103. http://dx.doi.org/10.1016/j.cageo.2013.01.021.

Fry, N., 1979. Random point distributions and strain measurement in rocks. Tectonophysics 60 (1), 89–105.

Fusseis, F., Xiao, X., Schrank, C., De Carlo, F., 2014. A brief guide to synchrotron radiation-based microtomography in (structural) geology and rock mechanics. J. Struct. Geol. 65, 1–16.

Gualda, G.A.R., Rivers, M., 2006. Quantitative 3D petrography using X-ray tomography: application to Bishop Tuff pumice clasts. J. Volcanol. Geotherm. Res. 154, 48–62.

Gualda, G.A., Pamukcu, A.S., Claiborne, L.L., Rivers, M.L., 2010. Quantitative 3D petrography using X-ray tomography 3: documenting accessory phases with differential absorption tomography. Geosphere 6 (6), 782–792. http://dx.doi.org/10.1130/GES00568.1.

Harris, J.E., 1973. The inhibition of diffusion creep by precipitates. Metal Sci. 7 (1), 1–6. http://dx.doi.org/10.1179/030634573790445514.

Heilbronner, R., 2010. Mapping texture domains in quartzite microstructures. J. Geol. Soc. India 75 (1), 160–170.

Heilbronner, R., Barrett, S., 2013. Image Analysis in Earth Sciences: Microstructures and Textures of Earth Materials. Springer.

Hencky, H., 1931. The law of elasticity for isotropic and quasi − isotropic substances by finite deformations. J. Rheol. (1929-1932) 2 (2), 169–176. http://dx.doi.org/10.1122/1.2116361.

Hext, G.R., 1963. The estimation of second-order tensors, with related tests and designs. Biometrika 50 (3–4), 353–373. http://dx.doi.org/10.1093/biomet/50.3-4.353.

Higham, N.J., 2008. Functions of Matrices: Theory and Computation. SIAM, Philadelphia.

Hubbell, J.H., Seltzer, S.M., 2004. Tables of X-Ray Mass Attenuation Coefficients and Mass Energy-absorption Coefficients (Version 1.4). National Institute of Standards and Technology, Gaithersburg, MD [Online] Available: http://physics.nist.gov/xaamdi.

Huddlestone-Holmes, C.R., Ketcham, R.A., 2005. Getting the inside story: using computed X-ray tomography to study inclusion trails in garnet porphyroblasts. Am. Mineral. Nov.-Dec. 90, ea1–ea17. http://dx.doi.org/10.2138/am.2005.1840.

Hu, Q., Ley, M.R., Davis, J., Hana, J.C., Frazier, R., Zhang, Y., 2014. 3D chemical segmentation of fly ash particles with X-ray computed tomography and electron probe microanalysis. Fuel 116 (15), 229–236. http://dx.doi.org/10.1016/j.fuel.2013.07.037.

Iassonov, P., Gebrenegus, T., Tuller, M., 2009. Segmentation of X-ray computed tomography images of porous materials: a crucial step for characterization and quantitative analysis of pore structures. Water Resour. Res. 45, W09415. http://dx.doi.org/10.1029/2009WR008087.

Iassonov, P., Tuller, M., 2010. Application of segmentation for correction of intensity bias in X-ray computed tomography images. Vadose Zone J. 9 (1), 187–191.

http://dx.doi.org/10.2136/vzj2009.0042.

Jelínek, V., 1978. Statistical processing of anisotropy of magnetic susceptibility measured on groups of specimens. Stud. Geophys. Geod. 22 (1), 50–62. http://dx.doi.org/10.1007/BF01613632.

Jerram, D.A., Higgins, M.D., 2007. 3D analysis of rock textures: quantifying igneous microstructures. Elements 3 (4), 239–245. http://dx.doi.org/10.2113/gselements.3.4.239.

Kansal, A.R., Torquato, S., Stillinger, F.H., 2002. Computer generation of dense polydisperse sphere packings. J. Chem. Phys. 117 (18), 8212–8218. http://dx.doi.org/10.1063/1.1511510.

Ketcham, R.A., 2005a. Three-dimensional grain fabric measurements using high-resolution X-ray computed tomography. J. Struct. Geol. 27 (7), 1217–1228.

Ketcham, R.A., 2005b. Computational methods for quantitative analysis of three-dimensional features in geological specimens. Geosphere 1 (1), 32–41. http://dx.doi.org/10.1130/GES00001.1.

Ketcham, R.A., Carlson, W.D., 2001. Acquisition, optimization and interpretation of X-ray computed tomographic imagery: applications to the geosciences. Comput. Geosci. 27 (4), 381–400. http://dx.doi.org/10.1016/S0098-3004(00)00116-3.

Ketcham, R.A., Ryan, T.M., 2004. Quantification and visualization of anisotropy in trabecular bone. J. Microsc. 213, 158–171. http://dx.doi.org/10.1111/j.1365-2818.2004.01277.x.

Lado, F., Torquato, S., 1990. Two-point probability function for distributions of oriented hard ellipsoids. J. Chem. Phys. 93 (8), 5912–5917. http://dx.doi.org/10.1063/1.459501.

Lindquist, W.B., Venkatarangan, A., Dunsmuir, J., Wong, T., 2000. Pore and throat size distributions measured from synchrotron X-ray tomographic images of Fontainebleau sandstones. J. Geophys. Res. 105 (B9), 21509–21527. http://dx.doi.org/10.1029/2000JB900208.

Liu, J., Regenauer-Lieb, K., Hines, C., Liu, K., Gaede, O., Squelch, A., 2009. Improved estimates of percolation and anisotropic permeability from 3-D X-ray microtomography using stochastic analyses and visualization. Geochem. Geophys. Geosyst. 10, Q05010. http://dx.doi.org/10.1029/2008GC002358.

Luding, S., 2004. Molecular dynamics simulations of granular materials. In: Hinrichsen, H., Wolf, D.E. (Eds.), The Physics of Granular Media. Wiley-VCH Verlag GmbH & Co. KGaA, Weinheim, FRG. http://dx.doi.org/10.1002/352760362X.ch13.

Lubachevsky, B., Stillinger, F.H., 1990. Geometric properties of random disk packings. J. Stat. Phys. 60 (5–6), 561–583.

Maätzler, C., 2002. Relation between grain-size and correlation length of snow. J. Glaciol. 48 (162), 461–466. http://dx.doi.org/10.3189/172756502781831287.

Maire, E., Withers, P.J., 2014. Quantitative X-ray tomography. Int. Mater. Rev. 59 (1), 1–43.

Mills, I.M., 1995. Unity as a Unit. Metrologia 31 (6), 537. http://dx.doi.org/10.1088/0026-1394/31/6/013.

Moler, C.B., 2008. Numerical Computing with MATLAB. SIAM, Philadelphia, ISBN 978-0-89871-660-3.

Mookerjee, M., Peek, S., 2014. Evaluating the effectiveness of Flinn's k-value versus Lode's ratio. J. Struct. Geol. http://dx.doi.org/10.1016/j.jsg.2014.08.008.

O'Connor, A., Mulchrone, K.F., Meere, P.A., 2009. WinDICOM: a program for determining inclusion shape and orientation. Comput. Geosci. 35 (6), 1358–1368. http://dx.doi.org/10.1016/j.cageo.2008.08.015.

Owens, W.H., 2000. Statistical applications to second-rank tensors in magnetic fabric analysis. Geophys. J. Int. 142 (2), 527–538. http://dx.doi.org/10.1046/j.1365-246x.2000.00174.x.

Panozzo Heilbronner, R., 1992. The autocorrelation function: an image processing tool for fabric analysis. Tectonophysics 212 (3), 351–370.

Press, W.H., Teukolsky, S.A., Vetterling, W.T., Flannery, B.P., 2007. Numerical Recipes 3rd Edition: the Art of Scientific Computing. Cambridge University Press, Cambridge.

Priestley, M.B., 1981. Spectral Analysis and Time Series. Academic Press, San Diego.

Rahl, J.M., Brandon, M.T., Deckert, H., Ring, U., Mortimer, N., 2011. Tectonic significance of ductile deformation in low-grade sandstones in the mesozoic Otago subduction wedge, New Zealand. Am. J. Sci. 311 (1), 27–62. http://dx.doi.org/10.2475/01.2011.02.

Ramsay, J.G., 1967. Folding and Fracturing of Rocks. McGraw-Hill Companies.

Ramsay, J.G., Huber, M.I., 1983. The Techniques of Modern Structural Geology, vol. 1. Academic Press, London.

Reeder, R.J., Lanzirotti, A., 2006. Accessing user facilities and making your research experience successful. Elements 2 (1), 31–35. http://dx.doi.org/10.2113/gselements.2.1.31.

Ring, U., Brandon, M.T., 1999. Ductile Deformation and Mass Loss in the Franciscan Subduction Complex: Implications for Exhumation Processes in Accretionary Wedges. In: Special Publication-geological Society of London, 154, pp. 55–86. http://dx.doi.org/10.1144/GSL.SP.1999.154.01.03.

Ring, U., Brandon, M.T., Ramthun, A., 2001. Solution-mass-transfer deformation adjacent to the Glarus Thrust, with implications for the tectonic evolution of the Alpine wedge in eastern Switzerland. J. Struct. Geol. 23, 1491–1505. http://dx.doi.org/10.1016/S0191-8141(01)00015-3.

Rivers, M.L., Sutton, S.R., Eng, P.J., 1999. Geoscience applications of x-ray computed microtomography. In: SPIE's International Symposium on Optical Science, Engineering, and Instrumentation International Society for Optics and Photonics, pp. 78–86.

Rivers, M.L., Citron, D.T., Wang, Y., 2010. Recent developments in computed tomography at GSECARS. In: SPIE Optical Engineering+ Applications, International Society for Optics and Photonics, p. 780409.

Ryan, T.M., Ketcham, R.A., 2002. The three-dimensional structure of trabecular bone in the femoral head of strepsirrhine primates. J. Hum. Evol. 43 (1), 1–26. http://dx.doi.org/10.1006/jhev.2002.0552.

Salavon, J., 1998. The Class of 1988 & the Class of 1967. Retrieved from. http://www.salavon.com.

Shepp, L.A., Logan, B.F., 1974. The Fourier reconstruction of a head section. Nucl. Sci. IEEE Trans. 21 (3), 21–43. http://dx.doi.org/10.1109/TNS.1974.6499235.

Shimamoto, T., Ikeda, Y., 1976. A simple algebraic method for strain estimation from deformed ellipsoidal objects. 1. Basic theory. Tectonophysics 36 (4), 315–337. http://dx.doi.org/10.1016/0040-1951(76)90107-4.

Skoge, M., Donev, A., Stillinger, F.H., Torquato, S., 2006. Packing hyperspheres in high-dimensional Euclidean spaces. Phys. Rev. E 74 (4), 041127. http://dx.doi.org/10.1103/PhysRevE.74.041127.

Spencer, A.J.M., 1980. Continuum Mechanics. Dover Publications, Mineola, N.Y.

Sutton, S.R., Bertsch, P.M., Newville, M., Rivers, M., Lanzirotti, A., Eng, P., 2002. Microfluorescence and microtomography analyses of heterogeneous earth and environmental materials. Rev. Mineral. Geochem. 49 (1), 429–483. http://dx.doi.org/10.2138/rmg.2002.49.8.

Svitelman, V., Dinariev, O., 2013. Geostatistical approach to the anisotropy analysis of 3D rock microtomographic models. Comput. Geosci. 57, 116–123. http://dx.doi.org/10.1016/j.cageo.2013.04.007.

Tabor, R.W., Cady, W.M., 1978. The Structure of the Olympic Mountains. In: Analysis of a Subduction Zone, vol. 1033. US Govt. Print. Off., Washington.

Torquato, S., 2002. Random Heterogeneous Materials: Microstructure and Macroscopic Properties. Springer, New York.

Torquato, S., Lado, F., 1991. Trapping constant, thermal conductivity, and the microstructure of suspensions of oriented spheroids. J. Chem. Phys. 94 (6), 4453–4462. http://dx.doi.org/10.1063/1.460635.

Torquato, S., Stell, G., 1982. Microstructure of two-phase random media. I. Then-point probability functions. J. Chem. Phys. 77 (4), 2071–2077. http://dx.doi.org/10.1063/1.444011.

Torquato, S., Stell, G., 1983. Microstructure of two-phase random media. III. The n-point matrix probability functions for fully penetrable spheres. J. Chem. Phys. 79 (3), 1505–1510. http://dx.doi.org/10.1063/1.445941.

Torquato, S., Stell, G., 1985. Microstructure of two-phase random media. V. The n-point matrix probability functions for impenetrable spheres. J. Chem. Phys. 82 (2), 980–987.

Wadsworth, J., Ruano, O.A., Sherby, O.D., 2002. Denuded zones, diffusional creep, and grain boundary sliding. Metall. Mater. Trans. A 33 (2), 219–229. http://dx.doi.org/10.1007/s11661-002-0084-7.

Wright, T.O., Platt, L.B., 1982. Pressure dissolution and cleavage in the Martinsburg Shale. Am. J. Sci. 282 (2), 122–135. http://dx.doi.org/10.2475/ajs.282.2.122.

Xu, W.F., Zhang, Y., Peng, L.M., Ding, W.J., Nie, J.F., 2015. Formation of denuded zones in crept Mg−2.5Gd−0.1Zr alloy. Acta Mater. 84 (1), 317–329. http://dx.doi.org/10.1016/j.actamat.2014.10.046.